Spatiotemporal control of cell cycle acceleration during axolotl spinal cord regeneration

Emanuel Cura Costa[1#], Leo Otsuki[2#], Aida Rodrigo Albors[3], Elly M. Tanaka[2] & Osvaldo Chara[1,4]*

[1] Systems Biology Group, Institute of Physics of Liquids and Biological Systems, National Scientific and Technical Research Council, University of La Plata, La Plata, Argentina.

[2] The Research Institute of Molecular Pathology (IMP), Vienna Biocenter (VBC), Vienna, Austria

[3] Neural Development Group, Division of Cell and Developmental Biology, School of Life Sciences, University of Dundee, Dundee, UK.

[4] Center for Information Services and High Performance Computing, Technische Universität Dresden, Dresden, Germany

[#] These authors contributed equally to this work

* Corresponding author:

Osvaldo Chara

Center for Information Services and High Performance Computing (ZIH), Technische Universität Dresden, Nöthnitzer Straße 46, 01187 Dresden, Germany. Tel. +49 351 463-38780, E-mail: osvaldo.chara@tu-dresden.de

Systems Biology Group (SysBio), Institute of Physics of Liquids and Biological Systems (IFLySIB), National Scientific and Technical Research Council (CONICET) and University of La Plata, Calle 59 N 789, 1900 La Plata, Argentina. Tel. +54 221 4233283 Ext: 26, E-mail: ochara@iflysib.unlp.edu.ar

Web: http://sysbioiflysib.wordpress.com/

Abstract:

Axolotls are uniquely able to resolve spinal cord injuries, but little is known about the mechanisms underlying spinal cord regeneration. We previously found that tail amputation leads to reactivation of a developmental-like program in spinal cord ependymal cells (Rodrigo Albors *et al.*, 2015), characterized by a high-proliferation zone emerging 4 days post-amputation (Rost *et al.*, 2016). What underlies this spatiotemporal pattern of cell proliferation, however, remained unknown. Here, we use modelling, tightly linked to experimental data, to demonstrate that this regenerative response is consistent with a signal that recruits ependymal cells during 85 hours after amputation within ~830 μm of the injury. We adapted FUCCI technology to axolotls (AxFUCCI) to visualize cell cycles in vivo. AxFUCCI axolotls confirmed the predicted appearance time and size of the injury-induced recruitment zone and revealed cell cycle synchrony between ependymal cells. Our modeling and imaging move us closer to understanding bona fide spinal cord regeneration.

Introduction

The axolotl (*Ambystoma mexicanum*) has the remarkable ability to regenerate the injured spinal cord (reviewed in Freitas, Yandulskaya & Monaghan, 2019; Tazaki *et al*, 2017; Chernoff *et al*., 2003), and thus represents a unique system to study the mechanisms of successful spinal cord regeneration. Key players in this process are the ependymal cells lining the central canal of the spinal cord, which retain neural stem cell potential throughout life (Becker, Becker & Hugnot, 2018).

In earlier studies, we found that spinal cord injury in the axolotl triggers the reactivation of a developmental-like program in ependymal cells, including a switch from slow, neurogenic to fast, proliferative cell divisions (Rodrigo Albors *et al*., 2015). We showed that in the uninjured spinal cord and in the non-regenerating region of the injured spinal cord, ependymal cells divide slowly, completing a cell cycle in 14.2 ± 1.3 days. In contrast, regenerating ependymal cells speed up their cell cycle and divide every 4.9 ± 0.4 days (Rodrigo Albors *et al*., 2015; Rost et al., 2016). By using a mathematical modeling approach, we demonstrated that the acceleration of the cell cycle is the major driver of regenerative spinal cord outgrowth and that other processes such as cell influx, cell rearrangements, and neural stem cell activation play smaller roles (Rost *et al*., 2016). We quantitatively analyzed cell proliferation in space and time and identified a high-proliferation zone that emerges 4 days after amputation within the 800 μm adjacent to the injury site and shifts posteriorly over time as the regenerating spinal cord grows (Rost *et al*., 2016)(Figure 1–figure supplement 1). What underlies this precise spatiotemporal pattern of cell proliferation in the regenerating axolotl spinal cord, however, remains unknown. Pattern formation phenomena occurring during development can be quantitatively reproduced by invoking morphogenetic signals spreading from localized sources (Morelli *et al*., 2012). It is thus conceivable that tail amputation triggers a signal that propagates or diffuses along the injured spinal cord to speed up the cell cycle of resident cells.

In this new study, we take a modelling approach supported by previous and new experimental data to unveil the spatiotemporal distribution that such a signal should have in order to explain the observed rate of spinal cord outgrowth in the axolotl. We generate a new transgenic axolotl that reports cell cycle phases to confirm several of our theoretical predictions *in vivo*. Together, our results provide new clues for when and where to search for the signal/s that may be responsible for driving successful spinal cord regeneration.

Results

Model of uninjured spinal cord

Taking into account the symmetry of the ependymal tube and that ependymal cells organize as a pseudo-stratified epithelium (Joven & Simon, 2018), we modeled the anterior-posterior (AP) axis of the spinal cord as a row of ependymal cells (see Computational methods section 1.1 for more details). We modeled ependymal cells as rigid spheres of uniform diameter and assumed that they can be either cycling or quiescent and defined the fraction of cycling cells as the growth fraction, *GF*. We modeled the proliferation dynamics of cycling cells as follows: we assumed that in the initial condition, each cycling cell is in a random coordinate along its cell cycle, where the initial cell cycle coordinate and the cell cycle length follow an exponential and a lognormal distribution, respectively. In the uninjured axolotl spinal cord, upon cell division, i) the daughter cells inherit the cell cycle length from the mother's lognormal distribution and ii) the daughter cells translocate posteriorly, displacing the cells posterior to them. This last feature of the model is the implementation of what we earlier defined as "cell pushing mechanism" (Rost *et al*., 2016). This model predicts that after a time of approximately one cell cycle length, mitotic events will occur along the AP axis and contribute to the growth of the spinal cord (Figure 1A).

Model of regenerating spinal cord

Next, we removed the most posterior cells of the tissue to model tail amputation and the regenerative response in the remaining cells (N_0) *in silico* (see Figure 1B and Computational methods section 1.1 for more details). We assumed that amputation triggers the release of a signal that spreads anteriorly from the injury site with constant speed along the AP axis, recruiting cells by inducing a change in their cell cycle. We established that cell recruitment stops at time τ, recruiting λ μm of cells anterior to the amputation plane. We notated the AP position of the most anterior cell recruited by the signal as $\xi(t)$, and called this the recruitment limit, such that $\xi(t = \tau) = -\lambda$. In the model, all cycling cells anterior to the cell located at $\xi(t)$ are not recruited and continue cycling slowly during the simulations (Figure 1–figure supplement 2). In contrast, cycling cells posterior to $\xi(t)$ are recruited at a time t within the interval $0 \leq t \leq \tau$ and irreversibly modify their cycling according to their cell cycle phase at the time of recruitment.

Because we previously demonstrated that the length of G2 and M phases do not change upon amputation (Rodrigo Albors *et al*., 2015), we assumed that cells in G2 or M within the recruitment zone will continue cycling as before (Figure 1C, Computational methods section 1.1.3). In contrast, because we showed that regenerating cells go through shorter G1 and S phases than non-regenerative cells (G1 shortens from 152 ± 54 hours to 22 ± 19 hours; S shortens from 179 ± 21 hours to 88 ± 9 hours, Rodrigo Albors *et al*., 2015), we reasoned that the signal instructs recruited cells to shorten G1 and S, effectively shortening their cell cycle.

To explain how ependymal cells may shorten G1 and S phase in response to the injury signal, we conceived a mechanism of G1 shortening in which a certain part of this cell cycle phase is skipped. We implemented this mechanism as follows (Figure 1C, Figure 1 – figure supplement 2, Computational methods section 1.1.1): if at the time of recruitment the cell is in G1, there are two possible coordinate transformations. If the cell cycle coordinate is located before the difference between the long (non-

104 regenerative) G1 length and the shortened (regenerative) G1 length, the cell clock is reset; *i.e.*, its
105 transformed cell cycle coordinate will be the beginning of the shortened G1 phase in the next simulation
106 step (immediately after G2 + M phases). In contrast, if the original cell cycle coordinate of the cell is
107 located after the difference between the long G1 length and the shortened G1 length, there is no
108 change in the time to enter into S phase. The difference between the long and short G1 lengths
109 constitutes a sort of threshold. If the G1 cell lies before this value, it skips and if it lies after, it continues
110 cycling as before. This mechanism of G1 skipping predicts a partial synchronization of the cell cycle as
111 cells transit through G1 (Figure 1 – figure supplement 2) – an important implication that we test
112 experimentally later.

113 Because all DNA must be duplicated prior to cell division, we considered a different mechanism
114 to model S phase shortening: if the cell cycle coordinate belongs to S at the moment of recruitment, the
115 new cell cycle coordinate of this cell will be proportionally mapped to the corresponding coordinate of a
116 reduced S phase in the next simulation step (Figure 1C, Figure 1 – figure supplement 2, Computational
117 methods section 1.1.2). For instance, if the recruited cell is 40% into its (long) S phase when the signal
118 arrives, it will be in the 40% of its shorter S phase in the next simulation step.

119 Daughter cells of recruited cells inherit short G1 and S phases from their mothers and
120 consequently have shorter cell cycle lengths (Figure 1C). Finally, we assumed that recruitment of a
121 quiescent cell would induce its progress from G0 to G1 after an arbitrary delay (Computational methods
122 section 1.1.4). To parametrize the cell phase durations of recruited and non-recruited cycling cells, the
123 growth fraction and cell geometry, we used our previous experimental data from regenerating and non-
124 regenerating regions of axolotl spinal cords (Rodrigo Albors *et al*., 2015)(Computational methods section
125 1.2 and Table 1).

126 The model predicts that if we wait a time similar to the short cell cycle length, we will observe
127 more proliferation posterior to ξ than anterior to it. In particular, if this model is correct, the prediction
128 for ξ (Figure 1B) should agree with the experimental curve of the switchpoint separating the region of
129 high proliferation from low proliferation along the AP axis of the axolotl spinal cord during regeneration
130 (Figure 1-figure supplement 1).

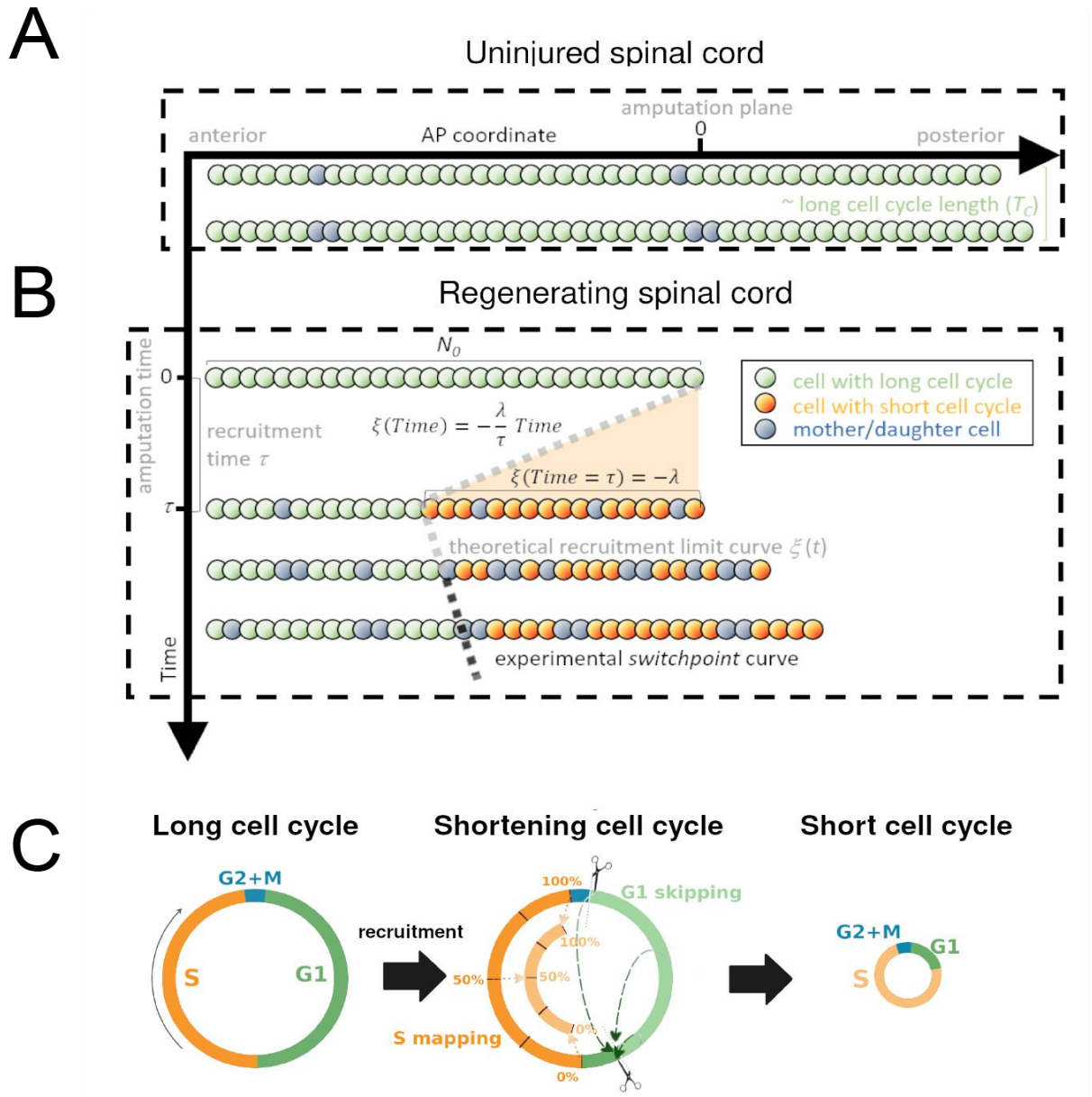

Figure 1. Model of uninjured and regenerating spinal cord growth based on shortening G1 and S cell phases. A) Uninjured spinal cord. 1D model of ependymal cells aligned along the AP axis. In uninjured tissue, ependymal cells cycle with long cell cycle length (see Figure 1 – figure supplement 1) and when they divide "push" cells posteriorly and the spinal cord tissue grows. As an example, two mother cells (in blue) in the top row give rise to four daughter cells in the second row (also in blue) following one division. This results in a growth of two cell diameters within a timeframe of approximately one long cell cycle length. **B) Regenerating spinal cord.** After amputation (AP coordinate and time equal to zero) a signal is released anteriorly from the amputation plane during a time τ and spreads while recruiting resident ependymal cells up to the theoretical recruitment limit ξ located at - λ µm from the amputation plane. After a certain time, the recruitment limit ξ overlaps the experimental switchpoint (see Figure 1 – figure supplement 1). **C) Proposed mechanisms of cell cycle shortening consists of partial skipping of G1 phase and proportional mapping between long and short S phases.** In the middle panel, two examples are depicted (dashed green arrows) of cells which were in the long G1 phase (immediately before recruitment) that become synchronized (immediately after recruitment). Additionally, there are three examples (dotted orange

arrows) of cells that were in the long S phase (immediately before recruitment) that are proportionally mapped (immediately after recruitment). All these examples are shown in detail in Figure 1 – figure supplement 2. The diameter of the circles is approximately proportional to the length of the cell's cell cycle.

Regenerative spinal cord outgrowth can be explained by a signal that acts during the 85 hours following amputation and recruits cells within 828 µm of the amputation plane

To evaluate if the model could explain the regenerative outgrowth of the ependymal tube and to estimate the free parameters, we fitted $\xi(t)$ to the experimental switchpoint (Rost *et al*., 2016). Specifically, we followed an inference Approximate Bayesian Computation method, streamlined by the use of pyABC-framework (Klinger, Rickert &Hasenauer, 2018). The model successfully reproduced the experimental switchpoint with best fitting parameters N_0 = 196 ± 2 cells, λ = 828 ± 30 µm and τ = 85 ± 12 hours (Figure 2A; parameter posterior distributions obtained after convergence are shown in Figure 2-figure supplement 1 and see computational methods section 1.3 for details). Interestingly, a clonal analysis of the model shows that while the anterior-most cells are slightly displaced, cells located close to the amputation plane end up at the posterior end of the regenerated spinal cord (Figure 2–figure supplement 2A), in agreement with cell trajectories observed during axolotl spinal cord regeneration (Rost *et al*., 2016). Additionally, the velocity of a clone monotonically increases with its AP coordinate (Figure 2–figure supplement 2B), also in line with experimental data (Rost *et al*., 2016). These results suggest that cells preserve their relative position along the AP axis. Hence, when plotting the relative position of each clone to the outgrowth of the corresponding tissue minus the recruitment limit $\xi(t)$, we observed that this normalized quantity is conserved in time, a fingerprint of the scaling behavior characteristic of regeneration (Figure 2–figure supplement 2C). Importantly, with the parameterization leading to the best fitting of the experimental switchpoint, we quantitatively predicted the time evolution of the regenerative outgrowth that was observed *in vivo* (Rost *et al*., 2016) (Figure 2B, Video 1).

Our model assumed that cells are rigid spheres of uniform diameter fixed from the mean length of ependymal cells measured along the AP axis (Rost *et al*., 2016). To test whether this *naïve* assumption could impact on our prediction of the regenerative spinal cord outgrowth, we repeated the simulations but replacing the mean cell length by the biggest and smallest possible cell lengths within a 99 % confidence interval based on earlier data (Rost *et al*., 2016). Spinal cord outgrowth predicted under these two extreme scenarios could hardly be distinguished from the previous prediction (Figure 2–figure supplement 3A, B). Similar results were obtained when we assumed that ependymal cells do not have a constant length along the AP axis but one extracted from a normal distribution parametrized from the experimental data on ependymal cell lengths along the AP axis (Figure 2–figure supplement 3C).

When we simulated a fast recruitment process by reducing the maximal recruitment time τ to one day while maintaining the maximal recruitment length λ constant, we found that the model-predicted outgrowth overestimates the experimental outgrowth (Figure 2–figure supplement 4A). On the contrary, when we decreased recruitment speed by increasing τ to 8 days while keeping λ constant, we observed a shorter outgrowth than that observed experimentally (Figure 2–figure supplement 4A). Reducing the maximal recruitment distance λ to zero mimics a hypothetical case in which the signal is

incapable of recruiting the cells anterior to the amputation plane (Figure 2-figure supplement 4B). Increasing λ by approximately 100 % without changing τ (that is, increasing recruitment speed) results in more recruited ependymal cells and faster spinal cord outgrowth than observed *in vivo* (Figure 2–figure supplement 4B). These results point to a spatially and temporarily precise cell recruitment mechanism underlying the tissue growth response during axolotl spinal cord regeneration.

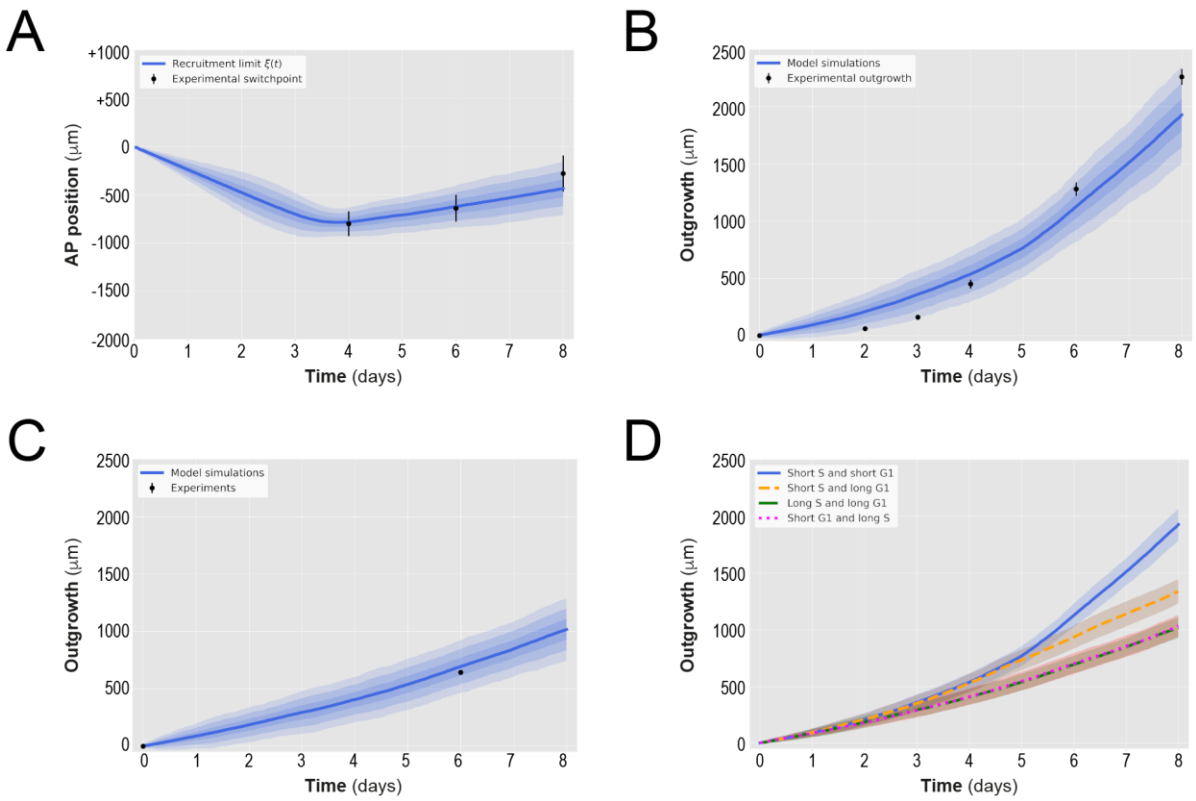

Figure 2. A hypothetical signal recruits ependymal cells up to 828 µm anterior to the amputation plane during the 85 hours following amputation, recapitulating *in vivo* spinal cord regenerative outgrowth. A) The modeled recruitment limit successfully fits the experimental switchpoint curve. Best fitting simulations of the model-predicted recruitment limit $\xi(t)$ overlap the experimental switchpoint curve. Best fitting parameters are N_0 = 196 ± 2 cells, λ = 828 ± 30 µm and τ = 85 ± 12 hours. **B) The model quantitatively matches experimental axolotl spinal cord outgrowth kinetics** (Rost *et al.*, 2016). **C) The model reproduces experimental outgrowth reduction when the acceleration of cell proliferation is impeded.** Prediction of the model assuming that neither S nor G1 phase lengths were shortened superimposed with experimental outgrowth kinetics in which acceleration of the cell cycle was prevented by knocking out *Sox2* (Fei *et al.*, 2014). Lines in A, B and C show the means while blue shaded areas correspond to 68, 95 and 99.7 % confidence intervals, from darker to lighter, calculated from the 1,000 best fitting simulations. **D) S phase shortening dominates cell cycle acceleration during axolotl spinal cord regeneration.** Spinal cord outgrowth kinetics predicted by the model assuming shortening of S and G1 phases (blue line), only shortening of S phase (orange dashed line), only shortening of G1 phase (magenta dotted line) and neither S nor G1 shortening (green line). The magenta line and green line are overlapped with one another. Means are represented as lines and each shaded area corresponds to one sigma out of 1,000 simulations.

209 **Regenerating spinal cord outgrowth when cell cycle acceleration is impeded**

210 We next asked how much the spinal cord would grow if the cell cycle acceleration instructed by the
211 injury signal is blocked. We made use of our model and predicted the tissue outgrowth when the lengths
212 of G1 and S were unaltered after amputation. In this condition, all cells would divide with the durations
213 of cell cycle phases reported under non-regenerating conditions (Rodrigo Albors *et al*., 2015). Our
214 results show that blocking recruitment, and therefore the acceleration of the cell cycle, slows down
215 tissue growth, leading to an outgrowth of 694 ± 77 μm instead of the observed 1,127 ± 103 μm at day 6
216 (Figure 2C). This result is consistent with reducing down to zero the maximal recruitment length λ
217 (Figure 2-figure supplement 4B). Interestingly, this model-predicted outgrowth is in agreement with the
218 reported experimental outgrowth in *Sox2* knock-out axolotls, in which the acceleration of the cell cycle
219 does not take place after amputation (Figure 2C, Fei *et al*., 2014).

220

221

222 **S phase shortening is sufficient to explain the initial regenerative spinal cord outgrowth**

223 The relative contributions of G1 *vs* S phase shortening to spinal cord outgrowth are an important
224 unknown that is technically difficult to interrogate *in vivo*. We made use of our model to answer this
225 question *in silico*. For this, we maintained the same parametrization recapitulating spinal cord
226 outgrowth (Figure 2A and B) but modified the model such that recruited cycling cells shorten S phase
227 but not G1 phase (*i.e.*, leaving unaltered G1 phase) or *vice versa*. Interestingly, our results indicate that
228 shortening of only S phase can explain the explosive spinal cord outgrowth observed *in vivo*,
229 independently of G1 shortening, up to day 4 (Figure 2D, blue line and orange line). In contrast,
230 shortening of only G1 phase has a mild impact on the initial outgrowth, as it results in an outgrowth
231 almost identical to the case in which neither G1 nor S phase were reduced (Figure 2D, magenta line
232 *versus* green line). From day 4, though, shortening of only S phase cannot recapitulate the observed
233 outgrowth (Figure 2D, blue line and orange line) and indeed, it is the shortening of both S and G1 phases
234 that returns the same outgrowth than that observed *in vivo*. These modeling predictions are a
235 consequence of i) the proximity of S phase to the next cell division compared with G1 phase ii) the fact
236 that S phase represents ~ 7.5 days of the total ~ 14 days of the long cell cycle, which is reduced to ~3.7
237 days in the ~5 days short cell cycle and iii) the time window of the investigated outgrowth was 8 days. To
238 conclude, these results indicate that, up to day 4, shortening of S phase can explain the regenerative
239 spinal cord outgrowth in the axolotl, while the effect of G1 shortening manifests from day 5.

240

241

242

243

244 **Visualizing cell cycle progression in axolotls *in vivo* using FUCCI**

245 Our model makes defined assumptions on how the phases of the cell cycle shorten to result in an
246 acceleration of cell cycle over 85 hours within 828 μm of the injury site. We sought to validate the model

247 by determining the kinetics of this response rigorously using a tool that distinguishes cell cycle phases *in*
248 *vivo* while preserving spatiotemporal context. For this, we adapted Fluorescent Ubiquitination-based
249 Cell Cycle Indicator (FUCCI) technology to axolotls (Figure 3A) (Zielke & Edgar, 2015). FUCCI is a
250 genetically encoded reporter that distinguishes cell cycle phases by capitalizing on the mutually
251 exclusive, oscillatory activity of two ubiquitin ligases (Sakaue-Sawano *et al.*, 2008). SCF^{Skp2} is active in S
252 and G2 of the cell cycle, when it targets the DNA licensing factor Cdt1 for proteolytic degradation. In
253 contrast, APC/C^{Cdh1} is active from mid-M to G1; during these phases, it targets Geminin (Gmnn; a Cdt1
254 inhibitor) for degradation. Fusing the degradation-targeting motifs (degrons) in the Cdt1 and Gmnn
255 proteins to two distinct fluorophores puts fluorophore abundance under the control of SCF^{Skp2} and
256 APC/C^{Cdh1} activity and enables fluorescence to be used as a readout for cell cycle phase. Importantly,
257 analyzing FUCCI does not require cell dissociation (thus preserving spatial context within the tissue),
258 immunostaining or measurement of DNA content.

259 FUCCI has been adapted successfully to several model organisms, including mouse, zebrafish,
260 *Drosophila* and human cells (reviewed by Zielke & Edgar, 2015). We designed axolotl FUCCI *de novo* by
261 extracting the degron-harboring sequences from the axolotl Cdt1 and axolotl Gmnn proteins. This was
262 important as we found that the N-terminus of Cdt1 protein, harboring the PIP degron, is divergent
263 across animal models (Figure 3-figure supplement 1A). We defined the relevant fragments of axolotl
264 Cdt1 protein (harboring the PIP degron and Cy motif) and axolotl Gmnn protein (harboring the D box
265 degron) using homology alignment and comparison with zebrafish FUCCI (Figure 3-figure supplements
266 1A,B,C,D) (Sugiyama *et al.*, 2009, Bouldin *et al.*, 2014). The axolotl $Cdt1_{[aa1-128]}$ fragment was fused to
267 mVenus fluorescent protein and the axolotl $Gmnn_{[aa1-93]}$ fragment to mCherry fluorescent protein. We
268 used the CAGGs ubiquitous promoter and viral T2A sequence to co-express the $Cdt1_{[aa1-128]}$-mVenus and
269 $Gmnn_{[aa1-93]}$-mCherry fusions in one transcript. The resulting axolotl-specific cell cycle reporter is referred
270 to as AxFUCCI (Figure 3A).

271

272

273

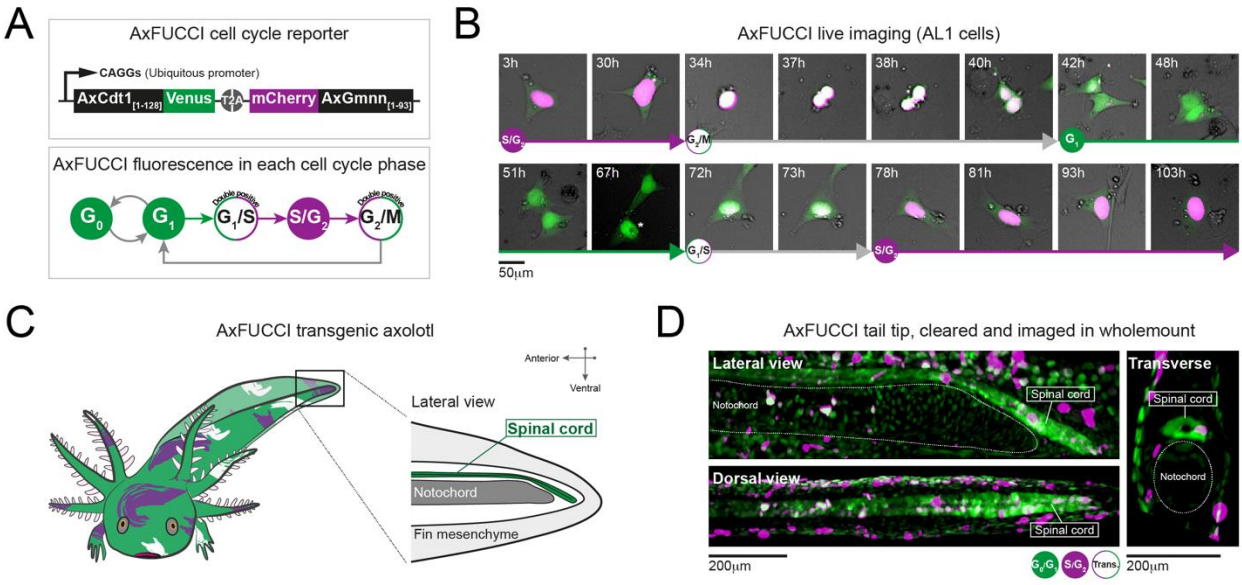

274

275 **Figure 3. AxFUCCI – a transgenic cell cycle reporter for axolotl. A) Top panel: AxFUCCI design.** A ubiquitous
276 promoter (CAGGs) drives expression of two AxFUCCI probes (AxCdt1[1-128]-Venus and mCherry-AxGmnn[1-93]) in
277 one transcript. The two AxFUCCI probes are separated co-translationally by virtue of the viral 'self-cleaving' T2A
278 peptide sequence. **Bottom panel: AxFUCCI fluorescence combinations in each phase of the cell cycle. B) Live**
279 **imaging of a single AxFUCCI-electroporated axolotl cell *in vitro*.** Each panel is a single frame acquired at the
280 indicated hour (h) after the start of the imaging session. One cell cycle (from S/G2 to the subsequent S/G2) is
281 depicted. At 67h, the two mitotic daughter cells moved apart; the asterisked daughter cell is depicted in the
282 remaining panels. **C) Establishment of AxFUCCI transgenic axolotls.** The location of the spinal cord is indicated in
283 the context of the tail. **D) A fixed AxFUCCI tail, cleared and imaged in wholemount using lightsheet microscopy.**
284 The 3D data enable *post-hoc* digital sectioning of the same spinal cord into lateral, dorsal or transverse views.
285 Images depict maximum intensity projections through 50 μm (lateral and transverse views) or 150 μm (dorsal
286 view) of tissue. Trans.: Transition-AxFUCCI (G1/S or G2/M transition).

287

288

289 **AxFUCCI discriminates cell cycle phases faithfully *in vivo***

290 We performed live cell imaging, DNA content analysis and immunofluorescence-based characterizations
291 to validate the ability of AxFUCCI to report the phases of the cell cycle. First, we electroporated an
292 immortalized axolotl cell culture line (AL1 cells) with AxFUCCI plasmid and performed live imaging. As
293 expected, AxFUCCI fluorescence oscillated during the cell cycle in the order mVenus > Double positive >
294 mCherry > Double positive > mVenus (Figure 3B, Figure 3-figure supplements 2A and B, Videos 2 and 3).
295 We confirmed that mVenus-positive cells were G0/G1 cells and that mCherry-positive cells were S/G2
296 cells using a flow cytometer to analyze DNA content (Figure 3-figure supplement 3A). Cells are
297 transiently AxFUCCI double positive between G0/G1 and S/G2 (Figure 3B and Figure 3-figure
298 supplements 2A,B); we infer that these cells are at the G1/S boundary, as observed in mouse FUCCI (Abe
299 *et al.* 2013). Interestingly, and in contrast to FUCCI in other model organisms, we observe a second
300 AxFUCCI double positive window between S/G2 and G0/G1, corresponding to the G2/M boundary and
301 M cells (Figure 3B and Figure 3-figure supplements 2A,B). Thus, AxFUCCI discriminates the following cell
302 cycle phases in axolotl: G0/G1 (mVenus only); S/G2 (mCherry only); G1/S transition and G2/M transition
303 (double positive) (Figure 3B). Importantly, AxFUCCI's capacity to label defined landmarks in the cell cycle
304 (*i.e.* G1/S and G2/M transition) enabled us to later test for cell cycle synchronization, a characteristic
305 feature of our model.

306 We generated stable transgenic AxFUCCI axolotls using I-SceI-mediated transgenesis, bred them
307 to sexual maturity and used F_1 (germline-transmitted) progeny for further validations (Figure 3C).
308 AxFUCCI animals developed at a similar rate to their non-transgenic siblings, did not differ in their basal
309 cell proliferation (Figure 3-figure supplement 4A) and regenerated amputated tail tissue with similar
310 kinetics to the *d/d* animals used in our previous study (Figure 3-figure supplement 4B). Cells dissociated
311 from AxFUCCI axolotl tails and analyzed using a flow cytometer exhibited the expected
312 fluorescence/DNA content relationships (Figure 3-figure supplement 4C). As a second assay, we
313 prepared spinal cord tissue sections from AxFUCCI axolotls and compared DNA content (as assessed by
314 DAPI fluorescence) in mVenus *vs* mCherry-positive cells. As expected, mCherry-positive cells harbored
315 significantly more DNA than mVenus-positive cells (Figure 3-figure supplement 4D,E). Thirdly, we
316 injected AxFUCCI axolotls intraperitoneally with EdU, a thymidine analogue that is incorporated into
317 DNA during S phase. Following an 8 hour EdU pulse, mCherry-positive cells but not mVenus-positive cells

318 should be EdU-positive and this was indeed the case (Figure 3-figure supplement 4F). Finally, we co-
319 stained AxFUCCI spinal cord tissue sections with cell type-specific markers. NeuN-expressing neurons,
320 located on the periphery of the spinal cord, are post-mitotic, differentiated cells (G0) and should be
321 mVenus-positive (and never mCherry-positive). Indeed, we found that 100% of neurons that expressed
322 AxFUCCI were mVenus-positive (Figure 3-figure supplement 4G). By contrast, Sox2-expressing
323 ependymal cells, which are proliferative cells, expressed mVenus, mCherry or both fluorophores (Figure
324 3-figure supplement 4H).

325 Based on these validations, and for simplicity, we refer to mVenus fluorescence as 'G0/G1-
326 AxFUCCI' (green in Figures 3-6), mCherry fluorescence as 'S/G2-AxFUCCI' (magenta in Figures 3-6) and
327 double positivity as 'Transition-AxFUCCI' (white in Figures 3-6).

328

329

330 **Measuring the recruitment zone *in vivo* using AxFUCCI**

331 We used AxFUCCI animals to measure the size of the ependymal cell recruitment zone *in vivo*. We
332 amputated AxFUCCI tails at 5 mm from the tail tips and harvested replicate regenerating tails daily up to
333 5 days post-amputation. We implemented a pipeline to optically clear and image fixed AxFUCCI tail
334 tissue in wholemount, which enabled *post-hoc* digital re-sectioning of the imaging data into any
335 orientation for accurate measurement (Figure 3D and Video 4) (Pende & Vadiwala *et al.*, 2020).
336 Importantly, this pipeline did not alter the length of the tail tissue (Figure 3-figure supplement 5). We
337 found that, at amputation, most ependymal cells expressed G0/G1-AxFUCCI and only a minority
338 expressed S/G2-AxFUCCI (Figure 4A). In the five days following tail tip amputation, the proportion of
339 S/G2-AxFUCCI-expressing cells increased locally and sharply at the amputation site, then propagated
340 anteriorly along the spinal cord, consistent with the appearance of a recruitment zone (Figure 4A and
341 Figure 1B).

342 As a first step, we quantified the percentage of ependymal cells expressing either G0/G1-
343 AxFUCCI alone or S/G2-AxFUCCI alone within the 1000-1600 μm of spinal cord anterior to the injury site
344 at each day post-amputation. A 1600 μm length should encompass not only the recruitment zone but
345 also more anteriorly located ependymal cells that are not recruited by the injury signal and that
346 continue to cycle slowly (Figure 1B). We performed our quantifications in 100 μm adjacent bins to
347 preserve spatial information, using the severed notochord tip to denote the amputation plane. To test
348 statistically whether the cells expressing G0/G1-AxFUCCI and S/G2-AxFUCCI are heterogeneously
349 distributed along the AP axis in the regenerating spinal cords (*i.e.* if a recruitment zone can be detected),
350 we followed an approach similar to that that we used previously to determine the switchpoint (Rost *et*
351 *al*., 2016). We fitted the measured spatial AP profiles of the percentage of G0/G1-AxFUCCI and S/G2-
352 AxFUCCI-expressing cells in each animal with a mathematical model assuming two adjacent
353 homogeneous spatial zones separated by an anterior-posterior border (AP border), which we assumed
354 was the same for both G0/G1 and S/G2-AxFUCCI data. For each animal at each time point, we tested if
355 the mean percentage of cells expressing G0/G1-AxFUCCI or S/G2-AxFUCCI in the anterior *versus* the
356 posterior zones were significantly different by running a Kolmogorov–Smirnov test. Up until 3 days post-
357 amputation, no statistical significance was detected between anterior and posterior in the G0/G1-
358 AxFUCCI and S/G2-AxFUCCI data (Figure 4B, Figure 4 -figure supplement 1A-D and Figure 4 -figure

359 supplement 2A-D). By contrast, at 4 and 5 days post-amputation, G0/G1-AxFUCCI and S/G2-AxFUCCI
360 data revealed a significant difference between the anterior and posterior zones, consistent with the
361 appearance of a recruitment zone (Figure 4B, Figure 4 -figure supplement 1E, F and Figure 4 – figure
362 supplement 2E,F).

363 Crucially, we measured the AP border of the AxFUCCI data to be at -717 ± 272 μm relative to
364 the amputation plane on day 4 and -446 ± 112 μm on day 5, overlapping within two sigma the -782 ± 50
365 μm and -710 ± 62 μm recruitment limits predicted by our model (Figure 4B). Moreover, the appearance
366 of the recruitment zone between days 3 and 4 post-amputation accommodates the 85 hour recruitment
367 time in our model. Thus, AxFUCCI animals confirmed the predicted appearance time and size of the
368 recruitment zone.

369

370

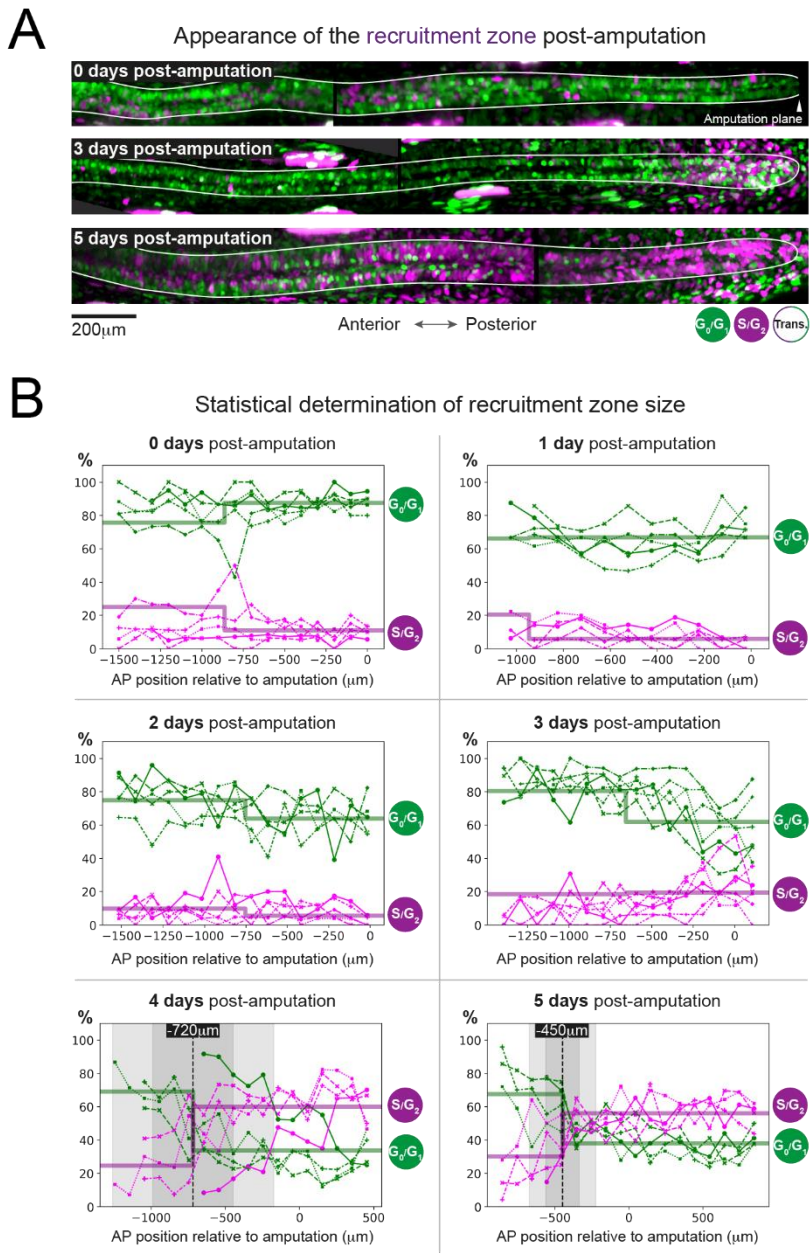

Figure 4. The predicted recruitment zone size is observed in AxFUCCI tails after amputation. A) Visualization of the recruitment zone in AxFUCCI tails. At amputation, most ependymal cells are G0/G1-AxFUCCI positive (green). After amputation, a decrease in G0/G1-AxFUCCI and an increase in S/G2-AxFUCCI (magenta) expression is seen anterior to the amputation plane and this zone increases in size anteriorly through day 5 post-amputation. The spinal cord is outlined. Images depict maximum intensity projections through 30 µm of tissue and are composites of two adjacent fields of view. **B) Quantification of the AP border that delimits the recruitment zone in G0/G1 and S/G2-AxFUCCI data.** Percentage of G0/G1 (in green) and S/G2 (in magenta)-AxFUCCI-expressing cells quantified in 100 µm bins along the anterior-posterior spinal cord axis. A mathematical model assuming two adjacent spatially homogeneous zones separated by an anterior-posterior border (AP border) was fitted to the G0/G1 and S/G2-AxFUCCI-data for each animal. Significant differences between anterior and posterior zones were detected only at day 4 and 5 (Kolmogorov-Smirnov test p = 0.0286). The AP border mean and two sigmas are depicted as a black dashed line and a grey shaded areas respectively. AP position is defined with respect to the

384 amputation plane (0 µm). *n* = 4-6 tails per time point, ~ 300 cells each. Different symbols depict different animals;
385 each line represents one animal. Best fitting values of the model regarding the anterior and posterior percentage
386 of AxFUCCI data is in Figure 4 – figure supplement 1. Individual fittings are in Figure 4 – figure supplement 2. For
387 more details, see Materials and Methods section 2.12.

388

389

390 **Regenerating cells have high cell cycle synchrony *in vivo***

391 Our model of G1 shortening (Figure 1C and Figure 1-figure supplement 2) predicts that ependymal cells
392 in the recruitment zone should exhibit high synchrony with each other in the cell cycle during early
393 regeneration, a property that has not been investigated. AxFUCCI axolotls enabled us to assess for
394 potential ependymal cell cycle synchrony in regenerating spinal cord.

395 We performed a more rigorous quantification of cell cycle distribution from our wholemount
396 data in which we focused on the 600 µm of spinal cord immediately anterior to the amputation plane,
397 within the recruitment zone, and also including Transition-AxFUCCI (G1/S and G2/M transition cells) and
398 M phase cells. At the moment of amputation, 85 ± 5 % of ependymal cells expressed G0/G1-AxFUCCI
399 and 11 ± 6 % expressed S/G2-AxFUCCI (Figure 5A). We note that this baseline differs from the one that
400 we reported previously in smaller, *d/d* control animals, but we found this lower basal proliferation rate
401 to be consistent among animals in this study independent of genotype (Figure 3-figure supplement 4A)
402 (Rodrigo Albors *et al*., 2015). Restrictions in feeding and/or changes in animal handling during the
403 COVID-19 pandemic might explain this difference (see Discussion). As we expected our model might be
404 robust to the baseline cell cycle profile, we gathered measurements in these animals for further
405 analysis.

406 After amputation, we detected a significant drop in G0/G1-AxFUCCI-expressing ependymal cells
407 already at day 1. Reciprocally, the number of S/G2-AxFUCCI-expressing cells increased significantly
408 starting at 3 days and reached 50 % at days 4 and 5 post-amputation, compared to a baseline
409 percentage below 10 % (Figures 5A and B). M phase cells started to appear noticeably from day 4,
410 although it was not possible to perform statistical analysis due to the absence of M phase cells in the 0
411 day post-amputation samples (Figure 5B). Intriguingly, we observed a transient and short 'burst' of
412 Transition-AxFUCCI cells at days 1 and 2 post-amputation. The percentage of Transition-AxFUCCI cells
413 increased to 21 ± 12 % and 23 ± 12 % respectively during this burst, before declining back to the
414 baseline level of 5 ± 4 % at 3 days (Figure 5B). We confirmed the accuracy of these quantifications by
415 preparing and quantifying tissue sections from replicate AxFUCCI spinal cords (Figure 5C and Figure 5-
416 figure supplement 1A).

417 Transition-AxFUCCI could correspond to G1/S transition or G2/M transition (Figure 3A). We
418 hypothesized that Transition-AxFUCCI cells at 1 and 2 days post-amputation resided at the G1/S
419 transition, as they appeared between the decline in G0/G1-AxFUCCI cells at day 1 and the increase in
420 S/G2-AxFUCCI cells at day 3. To confirm this, we subjected AxFUCCI animals to an EdU pulse for 24 hours
421 immediately prior to tail harvesting at 0, 1 or 2 days post-amputation. In this assay, Transition-AxFUCCI
422 cells that incorporate EdU should be in G2/M, while those that do not incorporate EdU should be in
423 G1/S (Figure 5-figure supplement 1B). Consistent with our expectations, Transition-AxFUCCI cells at 1

424 and 2 days post-amputation were almost entirely EdU-negative and therefore resided in G1/S (Figure 5D
425 and Figure 5-figure supplement 1C,D).

426 In sum, AxFUCCI revealed the following cell cycle dynamics during regeneration (summarized in
427 Figure 5E). Most ependymal cells in the uninjured spinal cord reside in G0/G1 phase of the cell cycle.
428 Following tail amputation, ependymal cells start to leave G0/G1 within the first day of amputation,
429 transit through G1/S at days 1 and 2, enter S/G2 from day 3 onwards and undergo mitosis from day 4.
430 The fact that these behaviors are readily observed at the population level indicates a high level of
431 synchrony among ependymal cells in the recruitment zone. The G1/S transition acts as a discrete
432 landmark in the cell cycle at which this synchrony can be inferred reliably. Transition-AxFUCCI cells are
433 very rare (~ 5 %) at amputation. We take the 4.5-fold increase in Transition-AxFUCCI-expressing cells at
434 days 1 and 2 post-amputation as a strong indication of cell cycle synchrony during early spinal cord
435 regeneration, a key prediction of our model.

436

437

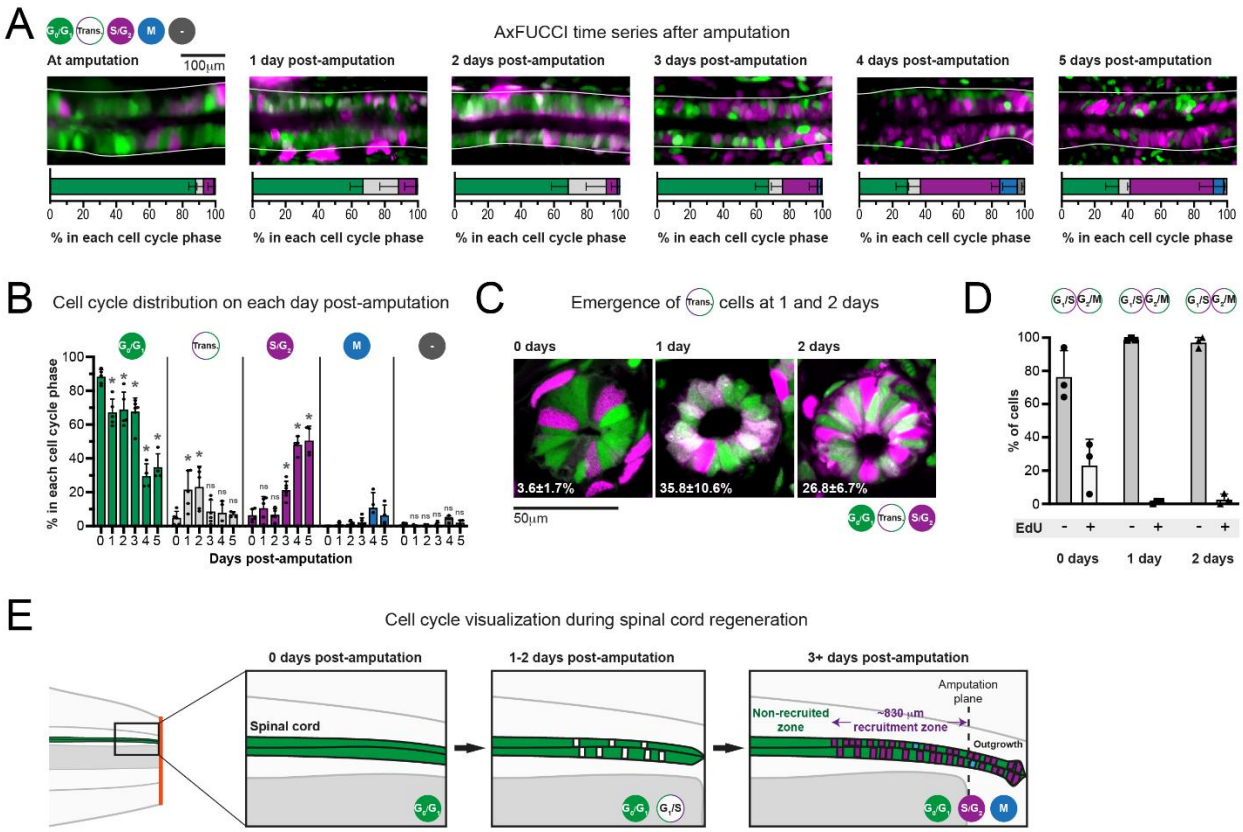

438

439 **Figure 5. Ependymal cells exhibit cell cycle synchrony during spinal cord regeneration. A) Cell cycle distributions**
440 **of ependymal cells during the first five days of regeneration.** Top row: maximum intensity projections through 25
441 μm of spinal cord oriented anterior to left and posterior to right. The spinal cord is outlined. The lumen is in the
442 center. Images were taken from within the 600 μm of most posterior regenerating spinal cord. Bottom row:

443 percentage of ependymal cells in each cell cycle phase in the 600 μm of most posterior regenerating spinal cord.
444 Cells in mitosis (M) were counted independently of AxFUCCI and were identified based on their condensed
445 chromatin as revealed by staining with DAPI (not shown). '-' indicates AxFUCCI-negative cells, which were
446 negligible at all time points. *n* = 4-6 tails per time point, ~ 100 cells each. Error bars indicate standard deviations. **B)**
447 **AxFUCCI data separated by cell cycle phase.** Quantitative data from panel A re-plotted by cell cycle phase. Day 0
448 data (immediately after amputation) were taken as baselines, and statistical analyses were performed against
449 these baselines. Kruskal-Wallis tests followed by Wilcoxon rank sum tests revealed a significant decrease in G0/G1-
450 AxFUCCI from 1 day post-amputation (p=0.02) and a significant increase in S/G2-AxFUCCI starting at 3 days post-
451 amputation (p = 0.02). One-way ANOVA followed by Tukey's HSD test revealed a significant increase in Transition-
452 AxFUCCI cells at 1 and 2 days post-amputation (p=0.04 and 0.02 respectively), but not at later days post-
453 amputation (p > 0.99). Mitotic cells were absent in the 0 day samples, precluding statistical analysis. The
454 percentage of AxFUCCI-negative cells was negligible and did not change at any time point (p = 0.40, Wilcoxon rank
455 sum). Each dot represents data from one tail. Error bars indicate standard deviations. ns: not statistically
456 significant. **C) The emergence of Transition-AxFUCCI cells at 1 and 2 days post-amputation was confirmed in**
457 **tissue sections.** Images are single plane confocal images of 10 μm-thick tissue cross sections fixed at the indicated
458 times after amputation. Percentages indicate the percentage of Transition-AxFUCCI cells at each time point (mean
459 ± standard deviation). *n* = 3 tails per time point, ~ 400 cells counted in each, corresponding to ~ 750 μm of spinal
460 cord. **D) Transition-AxFUCCI-expressing cells at 1 and 2 days post-amputation reside at the G1/S transition.**
461 Transition-AxFUCCI cells can be either at the G1/S transition or the G2/M transition. Following an 8 hour (0 days)
462 or 24 hour (1 and 2 days) EdU pulse, only G2/M cells should become labelled with EdU. Tails were fixed, then
463 processed for EdU detection and tissue sectioning. > 97 % of Transition-AxFUCCI cells were EdU-negative at 1 and 2
464 days post-amputation, indicating that they reside at the G1/S transition. *n* = 3 tails per time point. A total of 36,
465 442 and 315 Transition-AxFUCCI cells were assayed at 0, 1 and 2 days post-amputation respectively. **E) Cell cycle**
466 **dynamics during axolotl spinal cord regeneration.**

467

468

469 **A convergence in regenerative response from distinct baselines**

470 The AxFUCCI quantifications validated key predictions of our model in terms of the size of the
471 ependymal cell recruitment zone and in demonstrating high cell cycle synchrony during the regenerative
472 response. We were intrigued that these agreements occurred despite a significant difference in starting
473 cell cycle conditions (day 0) between the AxFUCCI animals and our model, which was based on data
474 described in (Rodrigo Albors *et al.* 2015). The AxFUCCI animals were of size 5.5 cm from snout to tail
475 and, on the day of amputation, 11 ± 6 % of ependymal cells expressed S/G2-AxFUCCI. In contrast, our
476 model was parametrized using measurements acquired from 3 cm, non-transgenic axolotls, in which the
477 baseline percentage of S-phase cells was four-fold higher, as inferred from cumulative BrdU labeling
478 (Rodrigo-Albors *et al.*, 2015). Despite these differences, we found the speed of spinal cord tissue
479 regeneration to be similar in the two datasets (Figure 3-figure supplement 4B). This could reflect a
480 convergence in regenerative response at the cell cycle level.

481 We investigated further the kinetics of this convergence by using our model to generate day-by-
482 day simulations of the spatial distribution of cells in G1 or S phase and comparing these simulations to
483 the cell cycle phase quantifications made from the AxFUCCI animals (Figure 6 A-D, Video 5). We
484 validated the simulations by testing where and when ependymal cells would leave G1 phase to enter S
485 phase and found that, as expected, simulated G1 to S transitions were more frequent posterior to the
486 experimentally derived recruitment limit (Figure 6 E), which at day 4 and 5 overlap with the determined

487 AP borders. Consequently, simulated cell divisions (M phase) exhibit a similar pattern (Figure 6 – figure
488 supplement 1).

489 We compared the model simulations to the AxFUCCI data. As noted, the cell cycle conditions at
490 day 0 differ between the AxFUCCI experiments and our model but match quantitatively at day 4 post-
491 amputation (Figure 6 A-D, Video 5). We found the appearance of the recruitment zone to be later in the
492 AxFUCCI animals (days 4-5) than in the simulations (day 2). However, once the recruitment zone is
493 evident in the AxFUCCI data, its size at day 4 and 5 is comparable to the one predicted by the
494 simulations at those times. Thus, the recruitment zone in the AxFUCCI spinal cord manifests more
495 synchronously and rapidly than in the simulations, in which it increases gradually in size in a posterior-
496 to-anterior direction from days 2 to 4. This is likely a consequence of the larger pool of G0/G1 cells in the
497 AxFUCCI animals at days 0-2 compared to the model, which incurs a collective (but relatively
498 synchronous) lag in S-phase entry (recruitment zone manifestation). Our data reveal two contrasting
499 trajectories towards achieving a common regenerative output.

500

501

502

503

504

505

506

507

508

509

510

511

512

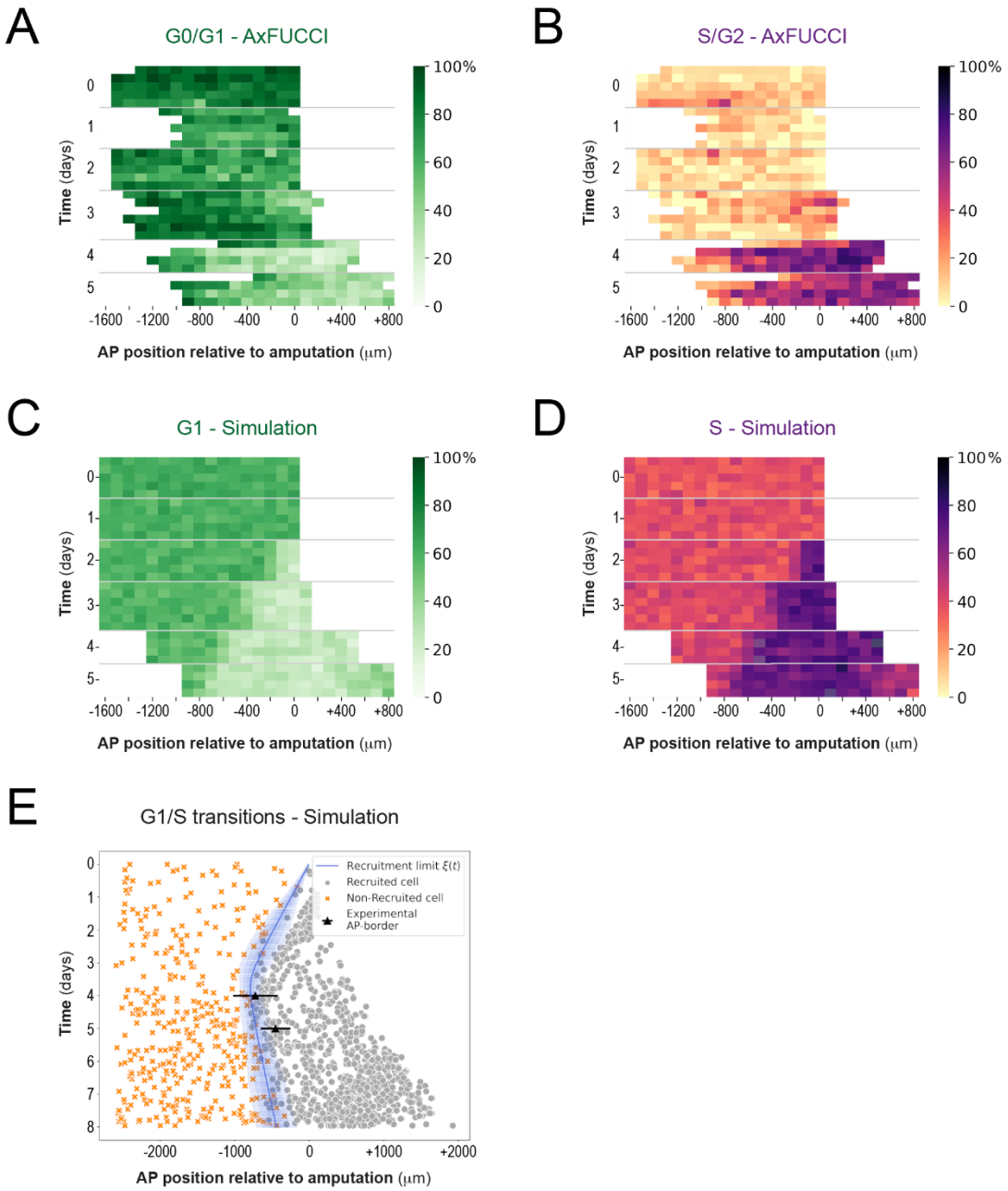

Figure 6. Convergence of cell cycle response between the model simulations and the AxFUCCI data. Heatmaps depicting spatiotemporal distribution of G0/G1-AxFUCCI cells **(A)**, S/G2-AxFUCCI cells **(B)**, model-predicted cells in G1 phase **(C)** and S phase **(D)**. x-axes depict AP position with respect to the amputation plane (AP position = 0 μm). y-axes depict time (days) post-amputation and both experimental and simulated replicates within each timepoint. The color codes correspond to the percentage of cells in the corresponding phase. Transition-AxFUCCI data are in Figure 6 – figure supplement 2. **(E)** Model-predicted occurrence of G1-S transitions is more often within the recruited (grey circles) compared to the non-recruited (orange crosses) cells. At days 4 and 5, the recruitment limit overlap with the AP borders. Independent simulations from 10 independent seeds are shown and the model is parameterized as in Figure 2.

523 **Discussion**

524 The tissue response to spinal cord injury differs greatly across vertebrates. In mammals, including
525 humans, injuries to the spinal cord often result in permanent tissue damage. In salamanders like the
526 axolotl, however, the ependymal cell response is tightly orchestrated to faithfully rebuild the missing
527 spinal cord (Joven & Simon, 2018; Tazaki, Tanaka & Fei, 2017). Following tail amputation, ependymal
528 cells in the axolotl spinal cord switch from slow, neurogenic to faster, proliferative cell divisions (Rodrigo
529 Albors *et al*., 2015). These faster cell cycles lead to the expansion of the ependymal/neural stem cell
530 pool and drive an explosive regenerative outgrowth. However, the mechanisms regulating cell cycle
531 dynamics during regeneration are not fully understood. Here, by using a modelling approach tightly
532 linked to experimental data, we find that the spatiotemporal pattern of cell proliferation in the
533 regenerating axolotl spinal cord is consistent with a signal that propagates anteriorly 828 um from the
534 injury site during the first 85 hours post-amputation. Although, for simplicity, we refer in this manuscript
535 to a single amputation-induced signal, our model could naturally extend to the combined output of
536 multiple genetic, chemical and/or biophysical signals. Moreover, we show that shortening of S phase is
537 sufficient to explain the explosive growth observed during the first days of regeneration, but that both S
538 and G1 shortening are necessary to explain/sustain further outgrowth before the first new-born neurons
539 are seen (Rodrigo Albors *et al*., 2015).

540 Compared to the number of mathematical models designed to unveil pattern formation
541 phenomena during development (Morelli *et al*., 2012), modelling in regeneration is still in its infancy
542 (Chara *et al*., 2014). An interesting example of modelling applied to regenerative processes was given by
543 a system of deterministic ordinary differential equations that was superbly used to disentangle how
544 secreted signaling factors could be used to control the output of multistage cell lineages in a self-
545 renewing neural tissue, the mammalian olfactory epithelium (Lander *et al*., 2009). Another
546 mathematical model based on ordinary differential equations was conceived to establish the causal
547 relationship between the individually quantified cellular processes to unravel the stem cell dynamics in
548 the developing spinal cord in chick and mouse (Kicheva *et al*., 2014). In a similar approach, we previously
549 modelled the regenerating axolotl spinal cord by means of a system of deterministic ordinary differential
550 equations describing the kinetics of the cycling and quiescent ependymal cell numbers which we
551 mapped to a model of spinal cord outgrowth (Rost *et al*., 2016). This allowed us to conclude that while
552 cell influx and cell cycle re-entry play a minor role, the acceleration of the cell cycle is the major driver of
553 regenerative spinal cord outgrowth in axolotls (Rost *et al*., 2016). A more recent study based on ordinary
554 and partial differential equations involving cell proliferation was used to predict the spinal cord growth
555 of the knifefish (Ilieş, Sipahi & Zupanc, 2018).

556 In this study, we investigated the spatiotemporal distribution of cell proliferation during axolotl
557 spinal cord regeneration. To do so, and in contrast with the aforementioned articles, we developed a
558 more general and yet accurate cell-based model introducing the spatial dimension relevant to the
559 problem: the AP axis. To further build a more realistic model, we included non-deterministic attributes:
560 an exponential distribution of the initial coordinates along the cell cycle and a lognormal distribution of
561 the cell cycle length. In the model, a signal shortens the cell cycle of ependymal cells along the AP axis as
562 a consequence of shortening their G1 and S phases, as we reported earlier (Rodrigo Albors *et al*., 2015).
563 Regulation of G1 and S phases are well-known mechanisms controlling cell fate and cell output in a
564 number of developmental contexts. In the brain, G1 lengthening results in longer cell cycles in neural
565 progenitors undergoing neurogenesis (Lukaszewicz *et al*., 2005; Calegari *et al*., 2005; Takahashi,

566 Nowakowski & Caviness, 1995), while experimental shortening of G1 in neural progenitors of the
567 cerebral cortex results in more proliferative divisions, increasing the progenitor pool and delaying
568 neurogenesis (Salomoni & Calegari, 2010; Lange, Huttner & Calegari, 2009; Pilaz *et al*., 2009; Calegari, F.
569 & Huttner, 2003). Here, we have shown that the shortening of G1 during spinal cord regeneration is
570 necessary to sustain the expansion of the ependymal cell pool. Together, these findings point to the
571 regulation of G1 length as a key mechanism regulating the output of neural stem/progenitor cell
572 divisions in development and in regeneration. The length of S phase is also regulated during
573 development by modulating the number of DNA replication origins (Nordman & Orr-Weaver, 2012). In
574 mammals, shortening of S phase seems to play a role in regulating the mode of cell division: mouse
575 neural progenitors committed to neurogenesis and neurogenic cortical progenitors in the ferret undergo
576 shorter S phase than their self-renewing/proliferative counterparts (Turrero García *et al*., 2016; Arai *et*
577 *al*., 2011). In the axolotl, regenerating ependymal cells shorten S phase during the expansion/outgrowth
578 phase. Together, these findings suggest that the regulation of S phase controls cell output in the context
579 of development and regeneration rather than influence the mode of cell division. The combined
580 shortening of S and G1 in the regenerating spinal cord sustains the expansion of the resident
581 ependymal/neural stem cell pool at the expense of neurogenesis. In this line, experimentally shortening
582 G1 and S phases in cortical progenitors of the developing mouse brain delayed the onset of
583 neurogenesis (Hasenpush-Theil *et al*., 2018). Our findings add to the evidence that cell cycle regulation is
584 a key mechanism controlling the number and type of cells needed to generate and regenerate a tissue.

585 Another prediction of our model is that a signal must spread about 800 μm from the injury site
586 while recruiting ependymal cells 85 hours after amputation to explain the spatiotemporal pattern of cell
587 proliferation in the regenerating spinal cord. In order to test this prediction experimentally, we adapted
588 FUCCI technology to axolotls, which enabled us to visualize cell cycle dynamics *in vivo*. We found
589 remarkable agreement between our prediction and the size and timing of appearance of the
590 recruitment zone in AxFUCCI spinal cords. Our prediction was made based on data from 3 cm snout-to-
591 tail axolotls, while the AxFUCCI measurements were taken from 5.5 cm axolotls. That the size of the
592 recruitment zone is constant between these two animal sizes could be important in understanding the
593 identity of the injury-induced signal and how it spreads to recruit ependymal cells. Future experiments
594 will determine if the size of the recruitment zone also remains constant in even larger axolotls.

595 A characteristic feature of our model is that G1 shortening after amputation causes ependymal
596 cells to partially synchronize with one another as they pass through G1. Cell cycle synchronization is
597 difficult to measure in cells *in vivo*. Here, AxFUCCI's property of labelling short, discrete landmarks in the
598 cell cycle (*e.g.* G1/S transition) enabled us to visualize high G1/S synchrony at 1 and 2 days post-
599 amputation *in vivo*. It will be interesting to assess whether a similar phenomenon occurs during
600 regeneration of other tissues in the axolotl (*e.g.* limb) and in other regenerative organisms.

601 Although we observed an excellent match between our model simulations and the AxFUCCI data
602 in terms of recruitment zone size at days 4 and 5 post-amputation, we also encountered quantitative
603 differences at earlier time points. In particular, we found that significantly fewer ependymal cells were
604 in S/G2 at baseline conditions in the present study compared to our previous study (Rost *et al*., 2016).
605 The AxFUCCI experiments reported here were carried out under COVID-19-related operational
606 restrictions – in particular, animal feeding frequency was reduced. A dietary reduction could plausibly
607 impact baseline ependymal cell proliferation rate and animal growth. We also cannot exclude an impact
608 from general housing conditions, as the previous experiments were performed in a different animal

609 facility with, for example, a different water supply. From the data analysis side, it is important to note
610 that in the AxFUCCI experiments, G0/G1 AxFUCCI cells become Transition AxFUCCI cells and then S/G2
611 AxFUCCI cells. This means that transition cells could be either cells in the late G1 or in the early S phases.
612 Modeled cells, in contrast, go straight from G1 to S phase. Consequently, we cannot quantitatively
613 equate the 'Transition phase' cells between experiments and model. This is why the AxFUCCI data and
614 the model simulations can only be qualitatively compared, especially at days 1 and 2, when transition
615 cells peak. Despite these considerations, we found that the proportions of ependymal cells in the G0/G1
616 *vs* S/G2 AxFUCCI data at 4 and 5 days post-amputation – *i.e*. during the first regenerative cell cycle –
617 accurately and quantitatively matched the simulations of our model. Moreover, the outgrowth rate of
618 the regenerating spinal cord was consistent between the AxFUCCI animals in this study and the animals
619 measured in our previous study (Figure 3-figure supplement 4B). This is to say that axolotls mount a
620 remarkably consistent regenerative response within their first cell cycle after amputation, possibly
621 converging their cell cycle responses despite differences in baseline. It will be fascinating to investigate
622 the molecular mechanisms that enable this consistent regenerative response in axolotls across age/size
623 and nutrition availability.

624 An important question now is whether the spatiotemporal cell cycle response observed in this
625 study agrees with known signaling events operating during spinal cord regeneration. A strong candidate
626 molecule for recruiting ependymal cells is the axolotl MARCKS-like protein (AxMLP), a secreted factor
627 involved in the proliferative response during axolotl appendage regeneration (Sugiura *et al*., 2016).
628 AxMLP is normally expressed in spinal cord cells but is upregulated following tail amputation, peaking 12
629 to 24 h after amputation and returning to basal levels a day later (Sugiura *et al*., 2016). The timing
630 prediction of our model is in agreement with the peak of AxMLP followed by a downstream period of
631 signal decoding to instruct intrinsic cellular changes that lead to faster cell cycles. Moreover, the
632 secreted nature of AxMLP protein could explain the long-range proliferative response in the
633 regenerating spinal cord. In the future, a tighter time-course characterization of AxMLP localization
634 throughout axolotl spinal cord regeneration will help to put our predictions to test.

635 Changes in the biophysical properties of the amputated tail could also trigger the orderly
636 increase in cell proliferation. In Xenopus tadpoles, tail amputation leads to the activation of the H+ V-
637 ATPase which is necessary and sufficient to promote tail regeneration (Adams *et al*., 2007). In the
638 axolotl, tail amputation triggers changes in calcium, sodium, and membrane potential at the injury site
639 (Ozkucur *et al*., 2010) while spinal cord transection induces a rapid and dynamic change in the resting
640 membrane potential which drives a c-Fos dependent gene expression program promoting a pro-
641 regenerative response (Sabin *et al*., 2015). The proliferation-inducing signal could also be of mechanical
642 nature (Chiou & Collins, 2018). In this direction, it is interesting that spinal cord transection in the
643 zebrafish induces an immediate alteration in the mechanical properties in the lesion site, which
644 gradually returns to normal (Schlüßler *et al*., 2018). Our predictions of the temporal and spatial
645 distribution that such proliferation-inducing signal could have will guide efforts to narrow down the
646 mechanisms responsible for successful spinal cord regeneration.

647 Taken together, our study provides a finer mechanistic understanding of the cell cycle kinetics
648 that drive spinal cord regeneration in axolotl and paves the way to search for the signal or signals that
649 launch the successful ependymal cell response to spinal cord injury.

650

651 **Materials and Methods**

652 **1. Computational methods**

653 **1.1 Model of developing and regenerating axolotl spinal cord**

654 We modeled the spinal cord as a densely packed row of ependymal cells. Since all the cells are assumed
655 identical rigid spheres, the model effectively involves only one spatial dimension: the anterior-posterior
656 (AP) axis of the spinal cord. We assumed that cells are either cycling or quiescent, where the fraction of
657 cycling cells is the growth fraction *GF*. We considered that each cycling cell *i* located in the position x_i at
658 the time *t* proliferates with a certain random cell cycle length lognormally distributed T_i (x_i, *t*) and has a
659 certain age within its cell cycle, C_i (x_i, *t*), defined as a coordinate along the cell cycle or clock ($0 \leq$
660 $C_i(x_i, t) < T_i(x_i, t)$). In the initial condition, each cycling cell has a random age $C_i(x_i, t = 0) = C_i^0$ along
661 its particular cell cycle length T_i (x_i, *t*), where the C_i^0 distribution is given by $\left(\frac{\ln 2}{T_i(x_i,t)}\right) 2^{1-\frac{2C_i^0}{T_i(x_i,t)}}$. As time *t*
662 goes by, each cycling cell increases its clock C_i (x_i, *t*) deterministically until it reaches its corresponding T_i
663 (x_i, *t*) value. At this precise moment, the cell divides and one daughter inherits its mother's AP
664 coordinate while the other is intercalated between the first daughter and the posterior neighboring cell.
665 This last feature of the model is the implementation of what we earlier defined as "cell pushing
666 mechanism" (Rost *et al*., 2016). After cell division, the daughter cells reinitiate their clocks and
667 $C_i(x_i, t) = 0$.This model predicts that after a time of approximately one cell cycle length, mitotic events
668 will occur along the AP axis, contributing to the growth of the spinal cord during development (Figure
669 1A).

670 To study the evolution of the tissue under a regenerative setup, we focused on the tissue
671 response to an amputation modeled by simply removing the most posterior cells. We modeled the
672 regenerative response in the remaining N_0 cells by assuming that amputation triggers the release of a
673 signal, which spreads with constant velocity anteriorly over the AP axis while recruiting the ependymal
674 cells. We assumed that cell recruitment stops at time τ, rendering λ μm of cells anterior to the
675 amputation plane recruited and a recruitment velocity $-\lambda/\tau$ during the interval $0 \leq t \leq \tau$. We notated
676 the AP position of the most anterior cell recruited by the signal as $\xi(t)$, the recruitment limit, such that
677 $\xi(t = \tau) = -\lambda$.

678 Because regenerative ependymal cells shorten G1 and S phases without altering G2 and M
679 phases leading to an acceleration of the cell cycle (Rodrigo Albors *et al*., 2015), we assumed that the
680 signal-induced recruitment instructs regenerating ependymal cells precisely to reduce G1 and S phases,
681 effectively shortening their cell cycle (Figure 1C). We represent here as $G1^{long}$ and S^{long} ($G1^{short}$ and S^{short})
682 the length of the corresponding phases for ependymal cells of uninjured animals (regenerating animals).
683 We notate with T^{long} and T^{short} to the cell cycle length of the ependymal cells in uninjured and
684 regenerating axolotls, respectively.

685 Note that a cycling cell *i* whose position x_i is anterior to the recruitment limit ($x_i < \xi(t)$) is not
686 recruited at time *t* and has a cell cycle length T_i (x_i,*t*) equal to T^{long}, that is, continue cycling slowly during
687 the simulations (Figure 1-figure supplement 1B). In contrast, a cycling cell *i* whose position x_i is posterior
688 to the recruitment limit ($x_i \geq \xi(t)$) within the time interval $0 < t \leq \tau$ is irreversibly recruited and
689 consequently has a cell cycle length T_i (x_i,*t*) equal to T^{short}. The progeny of the recruited cells (non

recruited cells) have a cell cycle length extracted from the same lognormal distribution of T^{short} (T^{long}) (Figure 1C).

We assumed that recruitment of a cell *i* located in the position x_i at time *t* induces an irreversible transformation in its cell cycle coordinate $C_i(x_i, t) \rightarrow C_i'(x_i, t)$, where C_i (x_i, *t*) and C_i' (x_i, *t*) are the original and transformed cell cycle coordinates, respectively. This means that the cell cycle coordinates of these cells undergo an irreversible coordinate transformation, modifying their cycling according to the cell cycle phase in which they are in at the moment of recruitment, as we describe the following subsections (Figure 1-figure supplement 1B):

1.1.1 When the cells are in the G1 phase at the time of recruitment

We assumed that if at the moment of amputation *t*, a cell *i* would be in a cell cycle coordinate C_i (x_i, *t*) within $0 \leq C_i(x_i, t) \leq G1^{long} - G1^{short}$, the new cell cycle coordinate is as follows (Figure 1C and Figure 1 – figure supplement 2):

$$C_i'(x_i, t) = 0 \qquad \text{(Eq. 1)}$$

which would induce a synchronization. In contrast, if at the moment of amputation *t*, a cell *i* would be in a cell cycle coordinate C_i (x_i, *t*) within $G1^{long} - G1^{short} \leq C_i(x_i, t) \leq G1^{long}$, the new cell cycle coordinate is:

$$C_i'(x_i, t) = C_i(x_i, t) - \left(G1^{long} - G1^{short}\right) \qquad \text{(Eq. 2)}$$

That is, these cells continue cycling as before. Taken together, the cells in G1 result partially synchronized (Figure 1C and Figure 1 – figure supplement 2).

1.1.2 When the cells are in the S phase at the time of recruitment

Taking into account that in S phase all DNA must be duplicated for cell division to occur, we considered a different mechanism to model S phase shortening based on proportional mapping. The new cell cycle coordinate of this cell are proportionally mapped to the corresponding coordinate of a shortened S phase in the next simulation step. Thus, we assumed that if at the moment of amputation *t*, a cell *i* would be in the S phase, that is, in a cell cycle coordinate C_i (x_i, *t*) within $G1^{long} \leq C_i(x_i, t) \leq G1^{long} + S^{long}$, the transformed cell cycle coordinate relative to the S phase length is invariant (Figure 1C and Figure 1 – figure supplement 2):

$$\frac{C_i'(x_i,t) - G1^{short}}{S^{short}} = \frac{C_i(x_i,t) - G1^{long}}{S^{long}} \qquad \text{(Eq. 3)}$$

As a consequence, the transformed cell cycle coordinate is as follows:

$$C_i'(x_i, t) = \left(C_i(x_i, t) - G1^{long}\right)\frac{S^{short}}{S^{long}} + G1^{short} \qquad \text{(Eq. 4)}$$

1.1.3 When the cells are either in the G2 or M phase at the time of recruitment

We previously demonstrated that sum of G2 and M phase lengths of the ependymal cells of axolotl spinal cords were conserved after amputation (Rodrigo Albors *et al.*, 2015). Hence, once a cell *i* is in the joint G2 + M phases, the remaining time to complete the cell cycle is the same for both, the original and the transformed cell cycle coordinates (Figure 1C):

$$T^{long} - C_i(x_i, t) = T^{short} - C_i'(x_i, t) \qquad \text{(Eq. 5)}$$

As a consequence, the transformed cell cycle coordinate can be calculated as follows:

$$C_i'(x_i, t) = C_i(x_i, t) + \left(T_C^{short} - T_C^{long}\right) \qquad \text{(Eq. 6)}$$

1.1.4 When the cells are in the G0 phase at the time of recruitment

We assumed that if a recruited cell *i* is quiescent at the moment *t* of recruitment, that is, in G0, it progress from this phase to the short-G1 phase after a certain delay $t_{G0\text{-}G1}$.

$$C_i'(x_i, t + t_{G0-G1}) = 0 \qquad \text{(Eq. 7)}$$

1.2 Model parametrization

The model parameters are summarized in Table 1. Briefly, the ependymal cell length along the AP axis, the distributions of cell phases durations and growth fraction were fixed from our previous publication (Rodrigo Albors *et al.*, 2015). The only free model parameters are the remaining anterior cells after amputation N_0, the maximal length λ along the AP axis of the putative signal and τ, the maximal time of cell recruitment.

1.3 Fitting procedure of the experimental switchpoint with the theoretical recruitment limit $\xi(t)$

The experimentally obtained switchpoint of the regenerating axolotl spinal cord (extracted from Rost *et al.*, 2016) was fitted with the model-predicted recruitment limit $\xi(t)$. We followed an Approximate Bayesian Computation method (ABC) to estimate the distribution of the parameters that better reproduces the experimental switchpoint data by our recruitment limit model. The ABC methods bypass the requirement for evaluating likelihood functions and capture the uncertainty in estimates of model parameters (Csilléry *et al.*, 2010). In particular, we used pyABC (Klinger, Rickert & Hasenauer, 2018), a high-performance framework implementing a Sequential Monte Carlo scheme (ABC-SMC), which provides a particularly efficient technique for Bayesian posterior estimation (Toni *et al.*, 2018).

Briefly, we generated a series of stochastic simulations from the model (described in the previous section) from sampled points of the parameter space. Each fitting run was initialized with a population size of 1000 samples. All the prior distributions of the parameters were defined as a discrete uniform distribution: N_0 ~ unif{100, 300}, λ ~ unif{500, 1500} and τ ~ unif{1,192}. Where the limits of τ were basically given by the entire experimental observation time (8 days) in hours. The limits of λ (in μm) and N_0 were initially estimated by previous simulation trials.

The sampled parameter values were accepted only when the distance function d between simulated recruitment limit and experimental switchpoint was lower than a given tolerance ε. The distance function was defined as follows:

$$d = \sqrt{\frac{\sum_i (x_i - \mu_i)^2}{{\sigma_i}^2}}. \qquad \text{(Eq. 8)}$$

where μ_i, σ_i and x_i correspond to the mean, standard deviation of the experimental switchpoint and the simulated recruitment limit, respectively, at the experimental time points i (4, 6 and 8 days). At each iteration, the parameter distributions were updated and re-sampled. The new tolerance ε was then calculated as the median of the distances from the last accepted sample population. The outcome of the algorithm was a sample of parameter values inferring their posteriors distributions (Figure 2–figure supplement 1A,B). Convergence of the method was assessed by following the value of ε and the acceptance rate, defined as the accepted number of simulations divided by the total number of simulations at each iteration step (Figure 2–figure supplement 1C,D).

1.4 Clones trajectories and velocities

We calculated the clone trajectories following the positions of each clone in random simulations. When a cell divided, we kept the mean position of the clone cells as the clone position. In Figure 2-figure supplement 2, a total of 11 tracks are shown, the first trajectory starts at 0 (the amputation plane) and the last at -1100 μm (with a sampling of 50 μm, approximately). To estimate the mean velocity of clones at different spatial positions in this model, the space along the AP axis was subdivided into 800 μm bins. For each clone trajectory, the positions were grouped according to these bins. Groups containing less than two measurements were excluded. The average clone velocity for each group was estimated with linear regression. Then, the mean and standard deviation of the velocity of all the clones in a bin was calculated.

1.5 Coordinate system

In all our simulations, the time starts with the event of amputation. Space corresponds to the anterior-posterior (AP) axis, where 0 represents the amputation plane and positive (negative) values are posterior (anterior) locations.

794 **1.6 Model implementation and computational tools**

795 The models were implemented in Python 3.0. Simulations and data analysis were performed using
796 Numpy (Oliphant, 2006) and Pandas (McKinney, 2010) while data visualization was executed with
797 Matplotlib (Hunter, 2007).

798

799

800 **1.7 Supplementary notebooks**

801 Jupyter Notebook (http://jupyter.org/) containing the source code for all computations performed and
802 referred to as Cura Costa *et al*., 2021 in this study can be found at
803 https://doi.org/10.5281/zenodo.4557840.

804

805

806 **2. Experimental materials and methods**

807 **2.1 Molecular biology**

808 AxFUCCI plasmid was constructed by standard restriction cloning. Relevant features of the AxFUCCI
809 plasmid are: (i) SceI site for stable transgenesis; (ii) CAGGs synthetic promoter for ubiquitous expression;
810 (iii) G0/G1-AxFUCCI probe (axolotl Cdt1[aa1-128]-GSAGSAAGSGEF glycine/serine linker-mVenus); (iv)
811 T2A 'self-cleaving' viral peptide; (v) S/G2-AxFUCCI probe (mCherry-SGGGGGSGGGGS glycine/serine
812 linker-axolotl Gmnn[aa1-93]); (vi) rabbit beta-globin polyadenylation sequence; (vii) SceI site for stable
813 transgenesis. PCR products were amplified using the primers listed in Table 2 and ligated in two rounds
814 into a vector already harboring SceI sites, a CAGGs promoter, a T2A sequence followed by mCherry and
815 rabbit beta-globlin polyadenylation sequence.

816 Primers were purchased as 20µM stocks (Sigma-Aldrich, standard de-salt). AxFUCCI plasmid sequence
817 was verified by Sanger sequencing.

818

819

820 **2.2 AL1 cell culture**

821 The immortalized axolotl 'AL1' cell line was grown in a humidified incubator at 25°C, with 2% CO_2. The
822 cell culture medium contains: 62.5% DMEM, 10% Fetal Bovine Serum, 25% water, supplemented with
823 100U Penicillin-Streptomycin, Glutamine, Insulin. AL1 cells were passaged every week at a ratio of 1:2
824 into gelatin-coated flasks.

825

826

827

828 **2.3 AL1 cell electroporation and live imaging**

829 Electroporation was performed using a Neon Transfection System (Thermo Fisher Scientific). 50,000 AL1
830 cells were electroporated with 1µg of AxFUCCI plasmid in 70% PBS/water using the following settings:
831 750V, 35ms pulse width, 3 pulses. Electroporated AL1 cells were plated onto a glass-bottomed Ibidi
832 imaging dish coated with gelatin. After two days, the cell culture medium was exchanged, and the dish
833 placed in a Celldiscoverer 7 automated live cell imaging microscope chamber (Zeiss). The microscope
834 chamber was maintained at 25°C, with 2% CO_2. Cells were imaged hourly over the course of 7 days for
835 Venus and mCherry fluorescence, and brightfield.

836

837

838 **2.4 Fluorescence intensity track measurements**

839 AxFUCCI fluorescence intensities were measured using the TrackMate plugin for FIJI (Tinevez, Perry &
840 Schindelin *et al.*, 2017). Fluorescence intensities were normalized to the maximum intensity observed
841 for the respective fluorophore during the experiment.

842

843

844 **2.5 DNA quantification by flow cytometry**

845 AxFUCCI-electroporated AL1 cells were incubated for 90 minutes with cell culture medium containing
846 10µg/ml Hoechst DNA stain. After incubation, AL1 cells were washed once with 70% PBS/water, then
847 dissociated into single cells using Trypsin. Dissociation was terminated by adding a 1:1 volume of serum-
848 containing cell culture medium. Cells were pelleted and re-suspended in 70% PBS/water, then filtered
849 through a 50µm cell filter. Cells were analysed for DNA content using a BD LSRFortessa Flow Cytometer
850 and FlowJo software.

851

852

853 **2.6 Axolotl husbandry and transgenesis**

854 d/d and AxFUCCI axolotls (*Ambystoma mexicanum*), snout-to-tail length 5.5cm, were raised in individual
855 aquaria. Axolotl breedings were performed by the IMP animal facility. All experiments were performed
856 in accordance with locally applicable ethics committee guidelines and within a framework agreed with
857 the Magistrate of Vienna (Genetically Modified Organism Office and MA58, City of Vienna, Austria).
858 Axolotls were anaesthetized with benzocaine (Sigma) diluted in tap water prior to amputation and/or
859 imaging.

860 AxFUCCI axolotls were generated by I-SceI meganuclease-mediated transgenesis using previously
861 described methods (Sobkow *et al.*, 2006). Briefly, one-cell stage fertilised d/d axolotl eggs were de-
862 jellied and injected with 5nl of injection mix (~0.5ng AxFUCCI plasmid and 0.005U I-SceI meganuclease
863 (NEB) diluted in 1X CutSmart buffer (NEB)). Injected axolotl eggs were maintained in 0.1X MMR/tap
864 water at room temperature until screening. Transgenic founder (F0) animals were identified by their

865 Venus fluorescence using an AXIOzoom V16 widefield microscope (Zeiss). F1 germline-transmitted
866 AxFUCCI animals were used for all experiments in this study. Sample sizes were determined empirically
867 and within the confines of experimentation under COVID19 pandemic-induced operational restrictions.

868

869

870 **2.7 Tissue clearing and lightsheet imaging**

871 AxFUCCI tails were fixed overnight at 4°C in 4% paraformaldehyde. Fixed tails were washed well with
872 PBS, then de-lipidated for 30 minutes at 37°C in Solution-1 of the DEEP-clear tissue clearing protocol
873 (10% v/v THEED, 5% v/v Triton X-100, 25% w/v urea in water) (Pende & Vadiwala *et al.*, 2020). De-
874 lipidated tails were washed with PBS, then incubated for 2 hours in PBS containing 10µg/ml DAPI. Tails
875 were washed well, then incubated overnight in Easyindex refractive index matching solution (LifeCanvas
876 technologies). Samples were kept dark at all times to prevent bleaching of AxFUCCI fluorescence.
877 Cleared AxFUCCI tails were imaged in EasyIndex solution using a LightSheet.Z1 microscope (Zeiss) and
878 custom chamber.

879

880

881 **2.8 Preparation of tissue sections**

882 AxFUCCI tails were fixed overnight at 4°C in 4% paraformaldehyde. Fixed tails were washed well with
883 PBS, then incubated overnight in 30% sucrose in PBS. The following day, samples were embedded in OCT
884 (Optimal Cutting Temperature) compound, frozen on dry ice and stored at -80°C until sectioning.
885 Cryosections of 10µm thickness were prepared from frozen blocks and stored at -20°C until use.

886

887

888 **2.9 Immunostaining and imaging of tissue sections**

889 Cryosections were warmed up to room temperature, then washed extensively with PBS to remove OCT.
890 Sections were blocked for 2 hours at room temperature with 10% normal goat serum (NGS) diluted in
891 PBS containing 0.2% Triton X-100 (PBTx). Blocked samples were incubated with primary antibody diluted
892 in 1% NGS overnight at 4°C. The following day, sections were washed well with PBTx, then stained with
893 Alexa Fluor-conjugated secondary antibodies diluted 1:500 in PBTx for 2 hours at room temperature.
894 DAPI was included in the secondary staining solution at a concentration of 10µg/ml. Sections were
895 washed well with PBTx and mounted in Mowiol containing 2.5% DABCO (Sigma). The following primary
896 antibodies were used in this study: anti-NeuN (Millipore MAB377, mouse, 1:500), anti-Sox2 (rabbit,
897 1:1,000, Fei *et al.*, 2016). Images were acquired using a LSM980 AxioObserver inverted confocal
898 microscope (Zeiss).

899

900

901

902 **2.10 EdU administration and detection**

903 Anaesthetized axolotls were injected intraperitoneally with 400µM EdU (diluted in PBS) at a dosage of
904 20µl/g. FastGreen dye (Sigma-Aldrich) was added to the injection mix to aid visualization. Injected
905 axolotls were kept out of water for a 20-minute recovery period under benzocaine-soaked towels. After
906 recovery, injected axolotls were returned to water. Following the desired pulse-chase period, axolotls
907 were sacrificed, tail tissue fixed and cryosections prepared.

908 EdU detection was performed using the Click-iT 647 EdU detection kit (Thermo Fisher Scientific)
909 according to the manufacturer's instructions.

910

911

912 **2.11 Image analysis**

913 Lightsheet data (AxFUCCI axolotl tails) were digitally re-sectioned or rendered in 3D using Imaris
914 software (Oxford Instruments). For quantification of wholemount data, spinal cords were digitally re-
915 sectioned longitudinally, to yield a continuous strip of spinal cord lumen, and images were exported as
916 TIFFs for cell counting in FIJI. Ependymal cells cell cycle phases were quantified from 25µm thick digital
917 sections. Ependymal cells were defined as cells in direct contact with the spinal cord lumen.
918 Celldiscoverer 7 videos (AL1 cells) were cropped using ZEN blue software (Zeiss), then analyzed using the
919 TrackMate plugin for FIJI, as described above. Tissue section images were analyzed and quantified using
920 FIJI software (Schindelin *et al.*, 2012).

921

922

923 **2.12 Determining the AP border between two adjacent spatial zones within axolotl regenerating**
924 **spinal cords**

925 We tested whether ependymal cells in the different cell cycle phases would be heterogeneously
926 distributed along the AP axis of the regenerating spinal cord. To that aim, we fitted the experimental
927 spatial AP profiles of the percentages of G0/G1-AxFUCCI and S/G2-AxFUCCI expressing cells, per animal,
928 with a mathematical model assuming two adjacent homogeneous spatial zones separated by an
929 anterior-posterior border, as follows:

930 $$g0g1(x) = \begin{cases} g0g1_a & if\ x < \text{AP border} \\ g0g1_p & if\ x \geq \text{AP border} \end{cases} \qquad \text{(Eq. 9)}$$

931

932 $$sg2(x) = \begin{cases} sg2_a & if\ x < \text{AP border} \\ sg2_p & if\ x \geq \text{AP border} \end{cases} \qquad \text{(Eq. 10)}$$

933 Where $g0g1(x)$ and $sg2(x)$ are the model variables describing the spatial distribution of G0/G1 and S/G2
934 cells along x, the spatial position along the AP-axis. The model parameters are $g0g1_a$, the anterior

935 percentage of G0/G1-AxFUCCI expressing cells, $g0g1_p$, the posterior percentage of G0/G1-AxFUCCI
936 expressing cells, $sg2_a$, the anterior percentage of S/G2-AxFUCCI expressing cells, $sg2_p$, the posterior
937 percentage of S/G2-AxFUCCI expressing cells and *AP border*, the border between the anterior and the
938 posterior zones, assumed equal for G0/G1-AxFUCCI and S/G2-AxFUCCI cells.

939 We fitted the model simultaneously to the AP profile of the percentage of G0/G1-AxFUCCI and S/G2-
940 AxFUCCI expressing cells of each animal and each time by using an Approximate Bayesian Computation
941 method (ABC, see Computational methods section 1.3 for more details of the computational
942 implementation). Each fitting was initialized with a constant population size of 1000 samples. The
943 parameters priors were defined as a discrete uniform between 0 and 100% for $g0g1_a$, $g0g1_p$, $sg2_a$ and
944 $sg2_p$. The prior for the *AP border* was also a discrete uniform covering all the measured positions along
945 the AP axis. The distance function between the experimental FUCCI data and the two-zones model was
946 defined as:

947 $$d = \sum_x \sqrt{\left(G0/G1_{exp}(x) - g0g1(x)\right)^2 + \left(S/G2_{exp}(x) - sg2(x)\right)^2} \qquad \text{(Eq. 11)}$$

948 Where $G0/G1_{exp}(x)$ and $S/G2_{exp}(x)$ are the percentage of G0/G1-AxFUCCI and S/G2-AxFUCCI expressing
949 cells, respectively, determined at the bin *x* of the spinal cord AP axis (for each animal and each time).

950 Each fitting procedure had a total of 30 iterations. Fitting results are shown in Figure 4B, Figure 4-Figure
951 supplement 1 and Figure 4-Figure supplement 2.

952 For each time, we compared the anterior *versus* the posterior zones of G0/G1-AxFUCCI and S/G2-
953 AxFUCCI data simultaneously by performing a Kolmogorov-Smirnov test between the best-fitting
954 parameters $g0g1_a$, $g0g1_p$ *versus* $sg2_a$, $sg2_p$. Although anterior and posterior zones were indistinguishable
955 from zero to 3 days post amputation, we found a significant difference between anterior and posterior
956 zones in the G0/G1-AxFUCCI and S/G2-AxFUCCI data at day 4 and 5 (Figure 4 – figure supplement 1). The
957 best fitting AP border detected for each time post-amputation are in Figure 4B as vertical gray areas at
958 day 4 and 5, post amputation.

959

960

961 **2.13 Statistical analysis and data representation**

962 In Figure 4, Kolmogorov-Smirnov test was implemented by using the Scipy (Virtanen *et al*., 2020) library.
963 Numpy's (Harris *et al*., 2020) high-level mathematical functions were used all along the simulations and
964 data analysis. In Figure 2 , Figure 2 - figure supplement 2, Figure 2 – figure supplement 3, Figure 2 –
965 figure supplement 4 and Figure 3 – figure supplement 4 B were made using Matplotlib (Hunter, 2007)
966 while Figure 4B, Figure 4 – figure supplement 1, Figure 4 – figure supplement 2, Figure 6, Figure 6 –
967 figure supplement 1 and Figure 6 – figure supplement 2 were performed with Seaborn (Waskom *et al*.,
968 2017). In Figure 5 and Figure 5-figure supplement 1, Figure 3-figure supplement 4, statistical analyses
969 were performed using R. AxFUCCI data were tested for assumptions of normality (Shapiro-Wilk test) and
970 equality of variance (Levene's test) in order to determine the appropriate statistical tests to perform. No
971 data were excluded. Details of statistical tests and their outcomes can be found in the relevant figure

legends. Statistical significance was defined as $p < 0.05$. These graphs were plotted using Prism (GraphPad). All the figures were compiled in Adobe Illustrator.

Acknowledgements

We thank Fabian Rost for critical comments on the manuscript. We also thank the members of the Chara lab and especially Alberto Ceccarelli for interesting discussions. We are grateful to Pietro Tardivo (tissue clearing and imaging), Anastasia Polikarpova (flow cytometry), Alberto Moreno-Cencerrado and Pawel Pasierbek (BioOptics facility, Vienna Biocenter) and the animal caretaker team (Vienna Biocenter), whose support enabled experiments to be performed during the COVID-19 pandemic.

Funding

This work was funded by Consejo Nacional de Investigaciones Científicas y Técnicas (CONICET) of Argentina and by the grants from Agencia Nacional de Promoción Científica y Tecnológica (ANPCyT), PICT-2014-3469, PICT-2017-2307 and PICT-2019-2019-03828 to O.C. E.C.C. was supported by a doctoral scholarship program from CONICET. O.C. is a career researcher from CONICET. A.R.A. was supported by the European Union's Horizon 2020 research and innovation programme under the Marie Skłodowska-Curie grant agreement No 753812. L.O. was supported by Human Frontier Science Program (HFSP) fellowship LT000785/2019-L. E.M.T acknowledges financial support from ERC Advanced Grant 742046, Special research programme (SFB) of the Austrian Science Fund (FWF): project F78 and institutional support from the IMP.

994 **References**

995 Abe T, Sakaue-Sawano A, Kiyonari H, Shioi G, Inoue K, Horiuchi T, Nakao K, Miyawaki A, Aizawa S & Fuji-
996 mori T. 2013. Visualization of cell cycle in mouse embryos with Fucci2 reporter directed by Rosa26
997 promoter. Development. 140:237–246.

998 Adams DS, Masi A & Levin M. 2007. H+ Pump-dependent changes in membrane voltage are an early
999 mechanism necessary and sufficient to induce Xenopus tail regeneration. Development. 34(7): 1323-35.

1000 Arai Y, Pulvers JN, Haffner C, Schilling B, Nüsslein I, Calegari F, Huttner WB. 2011. Neural stem and
1001 progenitor cells shorten S-phase on commitment to neuron production. Nat Commun. 2:154.

1002 Becker CG, Becker T, Hugnot JP. 2018. The spinal ependymal zone as a source of endogenous repair cells
1003 across vertebrates. Prog Neurobiol. 170: 67-80.

1004 Bouldin CM, Snelson CD, Farr GH 3rd & Kimelman D. 2014. Restricted expression of cdc25a in the tailbud
1005 is essential for formation of the zebrafish posterior body. Genes Dev. 28:384–395.

1006 Calegari F & Huttner WB. 2003. An inhibition of cyclin-dependent kinases that lengthens, but does not
1007 arrest, neuroepithelial cell cycle induces premature neurogenesis. J Cell Sci. 116: 4947–4955.

1008 Calegari F, Haubensak W, Haffner C, Huttner WB. 2005. Selective lengthening of the cell cycle in the
1009 neurogenic subpopulation of neural progenitor cells during mouse brain development. J Neurosci.
1010 25(28): 6533-8.

1011 Chara O, Tanaka EM & Brusch L. 2014. Mathematical modeling of regenerative processes. Curr Top Dev
1012 Biol. 108: 283-317.

1013 Chernoff EA, Stocum DL, Nye HL, Cameron JA. 2003. Urodele spinal cord regeneration and related
1014 processes. Dev Dyn. 226(2): 295-307.

1015 Chiou K & Collins ES. 2018. Why we need mechanics to understand animal regeneration. Dev Biol.
1016 433(2): 155-165.

1017 Csilléry K, Blum MGB, Gaggiotti OE & François O. 2010. Approximate Bayesian Computation (ABC) in
1018 practice. Trends in Ecology & Evolution. 25 (7): 410-418.

1019 Cura Costa E, Otsuki L, Rodrigo Albors A, Tanaka EM & Chara O. 2021. Spatiotemporal control of cell
1020 cycle acceleration during axolotl spinal cord regeneration - Supplementary notebooks – v2.0. Zenodo.
1021 https://doi.org/10.5281/zenodo.4557840

1022 Fei JF, Schuez M, Tazaki A, Taniguchi Y, Roensch K & Tanaka EM. 2014. CRISPR-mediated genomic
1023 deletion of Sox2 in the axolotl shows a requirement in spinal cord neural stem cell amplification during
1024 tail regeneration. Stem Cell Reports. 3(3): 444-59.

1025 Fei JF, Knapp D, Schuez M, Murawala P, Zou Y, Singh SP, Drechsel D & Tanaka EM. 2016. Tissue- and
1026 time-directed electroporation of CAS9 protein–gRNA complexes in vivo yields efficient multigene
1027 knockout for studying gene function in regeneration. npj Regen Med. 1(1): 16002.

1028 Freitas PD, Yandulskaya AS & Monaghan JR. 2019. Spinal Cord Regeneration in Amphibians: A Historical
1029 Perspective. Dev Neurobiol. 79(5): 437-452.

1030 Hasenpusch-Theil K, West S, Kelman A, Kozic Z, Horrocks S, McMahon AP, Price DJ, Mason JO, Theil T.
1031 2018. Gli3 controls the onset of cortical neurogenesis by regulating the radial glial cell cycle through
1032 Cdk6 expression. Development. 145(17).

1033 Harris CR, Jarrod Millman K, van der Walt SJ, Gommers R, Virtanen P, Cournapeau D, Wieser E, Taylor J,
1034 Berg S, Smith NJ, Kern R, Picus M, Hoyer S, van Kerkwijk MH, Brett M, Haldane A, Fernández del Río J,
1035 Wiebe M, Peterson P, Gérard-Marchant P, Sheppard K, Reddy T, Weckesser W, Abbasi H, Gohlke C &
1036 Oliphant TE. 2020. Array programming with NumPy, Nature, 585, 357–362. DOI:10.1038/s41586-020-
1037 2649-2

1038 Hunter JD. 2007. Matplotlib: A 2D graphics environment. Computing in Science & Engineering. 9:90–95.

1039 Ilieş I, Sipahi R & Zupanc GKH. 2018. Growth of adult spinal cord in knifefish: development and
1040 parametrization of a distributed model. Journal of Theoretical Biology. 437: 101–114.

1041 Joven A & Simon A. 2018. Homeostatic and regenerative neurogenesis in salamanders. Prog Neurobiol.
1042 170: 81-98.

1043 Kicheva A, Bollenbach T, Ribeiro A, Valle HP, Lovell-Badge R, Episkopou V & Briscoe J. 2014. Coordination
1044 of progenitor specification and growth in mouse and chick spinal cord. Science 345: 1254927.

1045 Klinger E, Rickert D, Hasenauer J. 2018. pyABC: distributed, likelihood-free inference. Bioinformatics.
1046 34(20): 3591-3593.

1047 Lander AD, Gokoffski KK, Wan FY, Nie Q & Calof AL. 2009. Cell lineages and the logic of proliferative
1048 control. PLoS Biol. 7(1): e15.

1049 Lange C, Huttner WB & Calegari F. 2009. Cdk4/cyclinD1 overexpression in neural stem cells shortens G1,
1050 delays neurogenesis, and promotes the generation and expansion of basal progenitors. Cell Stem Cell.
1051 5(3): 320-31.

1052 Lukaszewicz A, Savatier P, Cortay V, Giroud P, Huissoud C, Berland M, Kennedy H & Dehay C. 2005. G1
1053 phase regulation, area-specific cell cycle control, and cytoarchitectonics in the primate cortex. Neuron
1054 47: 353–364.

1055 McKinney W. 2010. Data structures for statistical computing in Python. Proceedings of the 9th Python in
1056 Science Conference: 51-56.

1057 Morelli LG, Uriu K, Ares S & Oates AC. 2012. Computational approaches to developmental patterning.
1058 Science. 336(6078): 187-91.

1059 Nordman J & Orr-Weaver TL. 2012. Regulation of DNA replication during development. Development
1060 139: 455-464.

1061 Oliphant TE. 2006. A guide to NumPy, USA: Trelgol Publishing.

1062 Ozkucur N, Epperlein HH & Funk RH. 2010. Ion imaging during axolotl tail regeneration in vivo. Dev Dyn.
1063 239(7): 2048-57.

1064 Pende M, Vadiwala K, Schmidbaur H, Stockinger AW, Murawala P, Saghafi S, Dekens MPS, Becker K,
1065 Revilla-i-Domingo R , Papadopoulos S-C, Zurl M, Pasierbek P, Simakov O, Tanaka EM, Raible F & Dodt HU.

1066 2020. A versatile depigmentation, clearing, and labeling method for exploring nervous system diversity.
1067 Sci Adv. 6: eaba0365.

1068 Pilaz LJ, Patti D, Marcy G, Ollier E, Pfister S, Douglas RJ, Betizeau M, Gautier E, Cortay V, Doerflinger N,
1069 Kennedy H & Dehay C. 2009. Forced G1-phase reduction alters mode of division, neuron number, and
1070 laminar phenotype in the cerebral cortex. Proc Natl Acad Sci U S A. 106(51): 21924-9.

1071 Rodrigo Albors A, Tazaki A, Rost F, Nowoshilow S, Chara O & Tanaka EM. 2015. Planar cell polarity-
1072 mediated induction of neural stem cell expansion during axolotl spinal cord regeneration. eLife. 4:
1073 e10230.

1074 Rost F, Rodrigo Albors A, Mazurov V, Brusch L, Deutsch A, Tanaka EM & Chara O. 2016. Accelerated cell
1075 divisions drive the outgrowth of the regenerating spinal cord in axolotls. eLife. 5. pii: e20357.

1076 Sabin K, Santos-Ferreira T, Essig J, Rudasill S & Echeverri K. 2015. Dynamic membrane depolarization is
1077 an early regulator of ependymoglial cell response to spinal cord injury in axolotl. Dev Biol. 408(1): 14-25.

1078 Sakaue-Sawano A, Kurokawa H, MorimuraT, Hanyu A, Hama H, Osawa H, Kashiwagi S, Fukami K, Miyata
1079 T, Miyoshi H, Imamura T, Ogawa M, Masai H & Miyawaki A. 2008. Visualizing spatiotemporal dynamics
1080 of multicellular cell-cycle progression. Cell. 132:487–498.

1081 Salomoni P & Calegari F. 2010. Cell cycle control of mammalian neural stem cells: putting a speed limit
1082 on G1. Trends Cell Biol. 20: 233–243.

1083 Schindelin J, Arganda-Carreras I, Frise E, Kaynig V, Longair M, Pietzsch T, Preibisch S, Rueden C, Saalfeld
1084 S, Schmid B, Tinevez J-Y, White DJ, Hartenstein V, Eliceiri K, Tomancak P & Cardona A. 2012. Fiji: an
1085 open-source platform for biological-image analysis. Nature Methods. 9: 676–682.

1086 Schlüßler R, Möllmert S, Abuhattum S, Cojoc G, Müller P, Kim K, Möckel C, Zimmermann C, Czarske J &
1087 Guck J. 2018. Mechanical Mapping of Spinal Cord Growth and Repair in Living Zebrafish Larvae by
1088 Brillouin Imaging. Biophys J. 115(5): 911-923.

1089 Sobkow L, Epperlein HH, Herklotz S, Straube WL & Tanaka EM. 2006. A germline GFP transgenic axolotl
1090 and its use to track cell fate: dual origin of the fin mesenchyme during development and the fate of
1091 blood cells during regeneration. Dev. biol. 290:386-397.

1092 Sugiura T, Wang H, Barsacchi R, Simon A & Tanaka EM. 2016. MARCKS-like protein is an initiating
1093 molecule in axolotl appendage regeneration. Nature. 531(7593): 237-40.

1094 Sugiyama M, Sakaue-Sawano A, Iimura T, Fukami K, Kitaguchi T, Kawakami K, Okamoto H, Higashijima S
1095 & Miyawaki A. 2009. Illuminating cell-cycle progression in the developing zebrafish embryo. Proc Natl
1096 Acad Sci USA. 106:20812–20817.

1097 Takahashi T, Nowakowski RS & Caviness VS Jr. 1995. The cell cycle of the pseudostratified ventricular
1098 epithelium of the embryonic murine cerebral wall. J Neurosci. 15(9): 6046-57.

1099 Tazaki A, Tanaka EM & Fei JF. 2017. Salamander spinal cord regeneration: The ultimate positive control
1100 in vertebrate spinal cord regeneration. Dev Biol. 432(1): 63-71.

1101 Tinevez JY, Perry N, Schindelin J, Hoopes GM, Reynolds GD, Laplantine E, Bednarek SY, Shorte SL &
1102 Eliceiri KW. 2017. TrackMate: An open and extensible platform for single-particle tracking. Methods.
1103 115:80-90.

1104 Toni T, Welch D, Strelkowa N, Ipsen A, Stumpf MP. 2009. Approximate Bayesian computation scheme
1105 for parameter inference and model selection in dynamical systems. J R Soc Interface. 6(31): 187-202.

1106 Turrero García M, Chang Y, Arai Y & Huttner WB. 2016. S-phase duration is the main target of cell cycle
1107 regulation in neural progenitors of developing ferret neocortex. J Comp Neurol. 524(3): 456-70.

1108 Virtanen P, Gommers R, Oliphant TE, Haberland M, Reddy T, Cournapeau D, Burovski E, Peterson P,
1109 Weckesser W, Bright J, van der Walt SJ, Brett M, Wilson J, Jarrod Millman K, Mayorov N, Nelson ARJ,
1110 Jones , Kern R, Larson E, Carey CJ, Polat İ, Feng Y, Moore EW, VanderPlas J, Laxalde D, Perktold J,
1111 Cimrman R, Henriksen I, Quintero EA, Harris CR, Archibald AM, Ribeiro AH, Pedregosa F, van Mulbregt P,
1112 and SciPy 1.0 Contributors. 2020. SciPy 1.0: Fundamental Algorithms for Scientific Computing in Python.
1113 Nature Methods, 17(3), 261-272.

1114 Waskom M, Botvinnik O, O'Kane D, Hobson P, Lukauskas S, Gemperline DC, Augspurger T, Halchenko Y,
1115 Cole JB, Warmenhoven J, de Ruiter J, Pye C, Hoyer S, Vanderplas J, Villalba S, Kunter G, Quintero E,
1116 Bachant P, Martin M, Meyer K, Miles A, Ram T, Yarkoni T, Lee Williams M, Evans C, Fitzgerald C, Brian,
1117 Fonnesbeck C, Lee A, Qalieh A. https://doi.org/10.5281/zenodo.883859

1118 Zielke N & Edgar BA. 2015. FUCCI Sensors: powerful new tools for analysis of cell proliferation. WIREs
1119 Dev Biol. 4:469-487.

1120

1121 **Supplementary Figures**

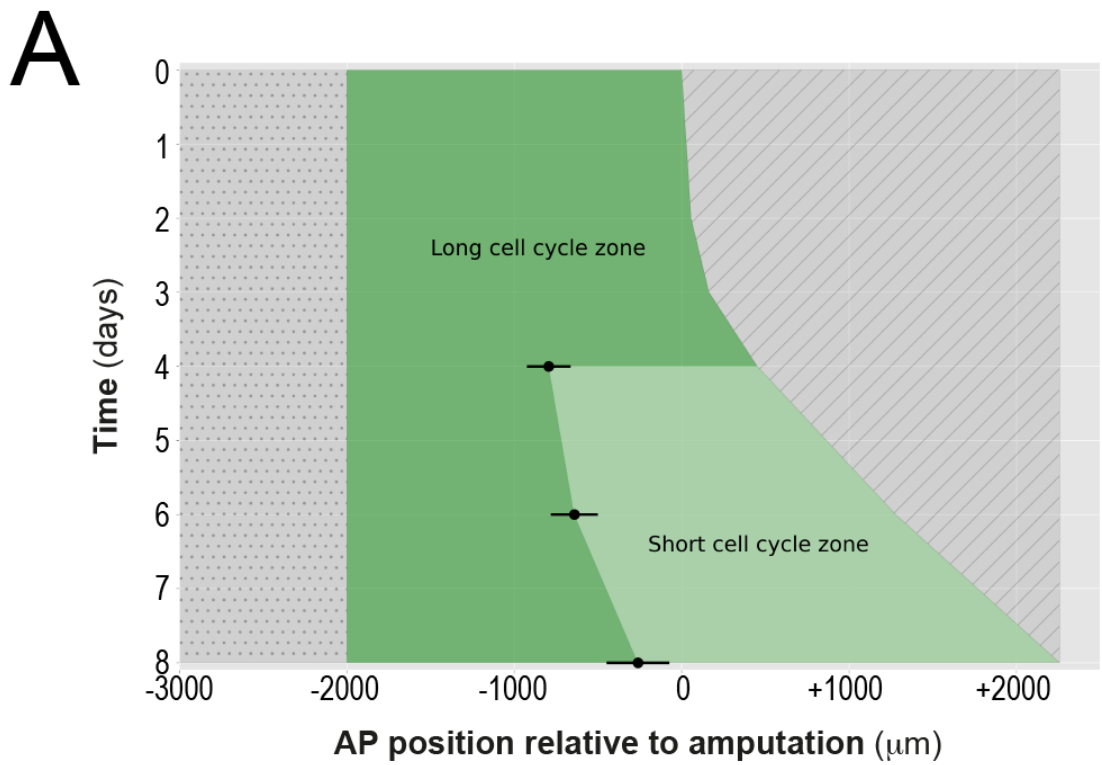

1122

1123

1124 **Figure 1-figure supplement 1. Space-time distribution of cell proliferation during axolotl spinal cord**
1125 **regeneration.** Experimental switchpoint (black dots) separating areas of low cell proliferation (Long cell cycle zone,
1126 dark-green) from high cell proliferation (short cell cycle zone, light-green) along the anterior-posterior (AP) axis
1127 (depicted horizontally) of the axolotl spinal cord. The dashed region marks the space outside of the embryo while
1128 the dotted region marks the unaffected part of the embryo (adapted from Fig.2 F'' of Rost *et al*., 2016). Each
1129 switchpoint value was determined as the border separating two spatially homogeneous zones assumed by a
1130 mathematical model, which was fitted to the experimental spatial distribution of growth fraction and mitotic index
1131 along the axolotl spinal cords (Rost *et al*., 2016).

1132

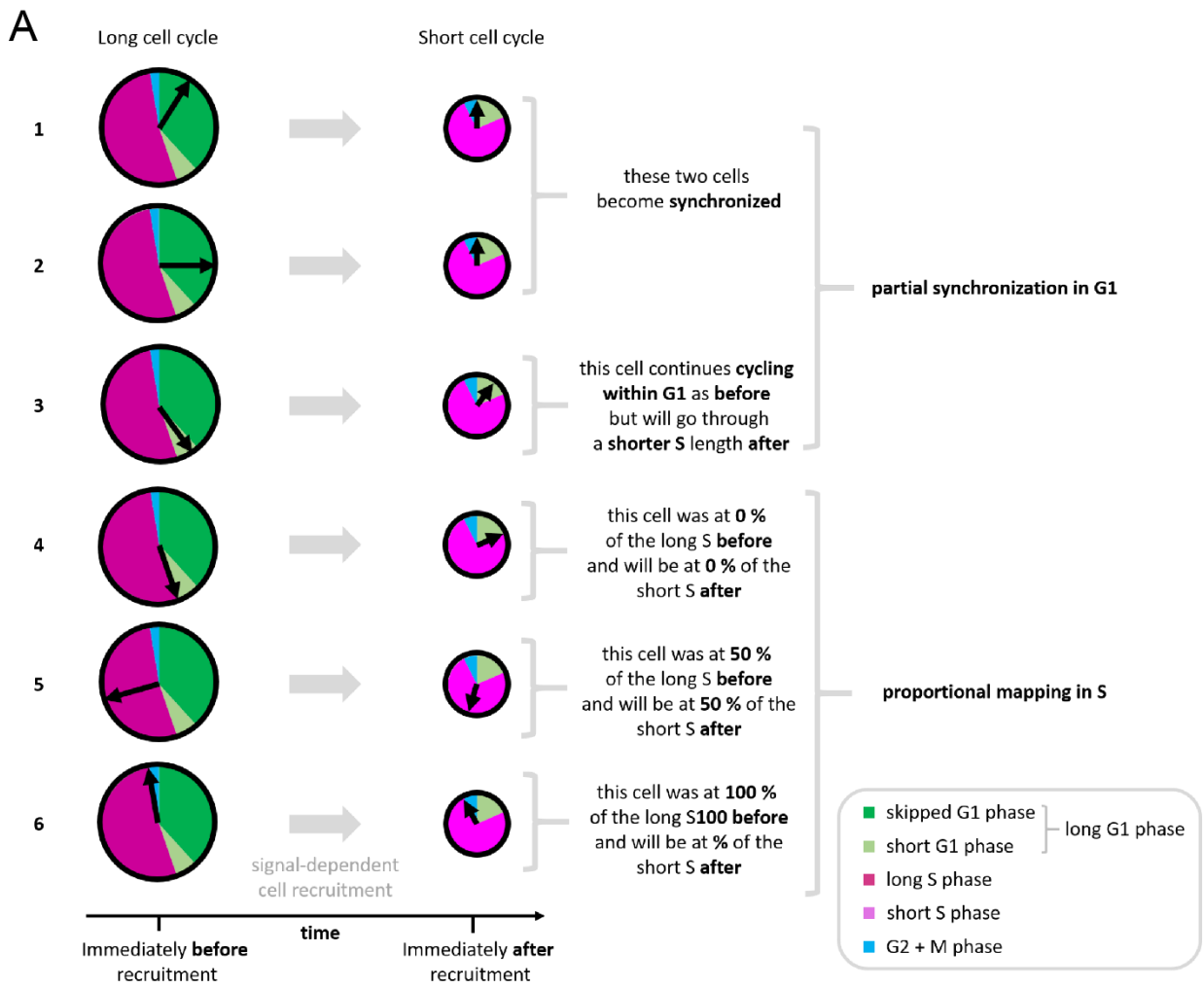

Figure 1-figure supplement 2. Further explanation of the cell cycle coordinate transformation invoked by the model. Cells in G1 phase at the moment of recruitment can skip the remainder of the phase, depending on where they are located in the long G1 phase. If their cell cycle coordinate is before the difference between the long and the short G1 phases, they skip this initial part of the long G1 phase and synchronize at the beginning of the short G1 phase **(1, 2)**. If their cell cycle coordinate is equal or after the difference between the long and the short G1 phases, they continue cycling as before, but they will go through a short S phase afterwards **(3)**. This generates a partial synchronization mechanism (See computational methods section 1.1.1). If the cells are in S phase at the moment of recruitment, cells follow a proportional mapping **(4 - 4)**. Essentially the cell cycle coordinates within S are scaled into the short S phase (See computational methods section 1.1.2).

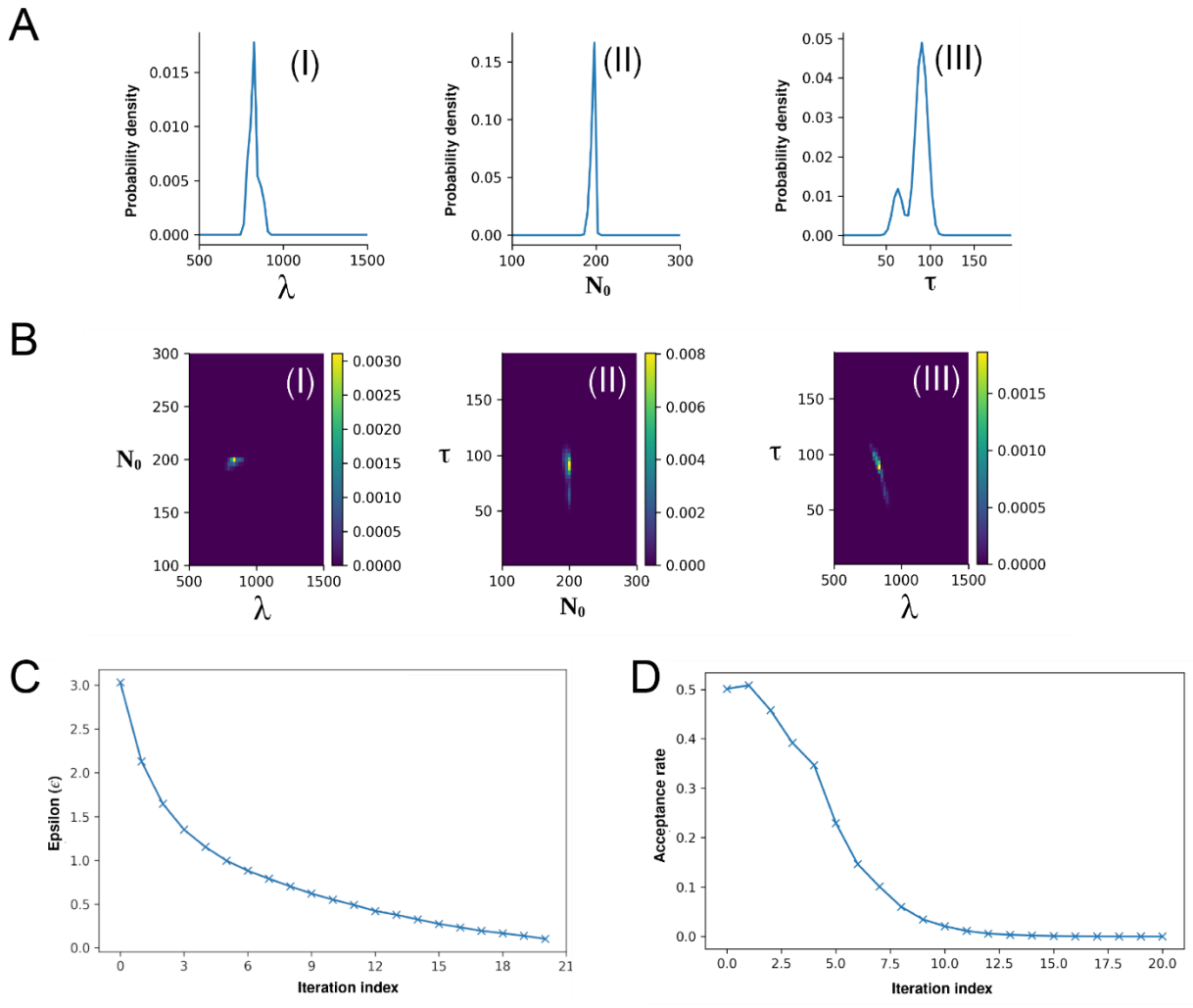

Figure 2-figure supplement 1. Approximate Bayesian Computation (ABC) fitting of the recruitment limit model to the experimental switchpoint data. (A) Posterior distributions of the parameters λ (I), N_0 (II) and τ (III). **(B).** Combined posterior distributions of N_0 and λ (I), τ and N_0 (II) as well as τ and λ (III). **(C and D)** Fitting process convergence depicted by the fitting tolerance ε (B) and the acceptance rate (D) *versus* the iteration index. (See computational methods section 1.3 for details).

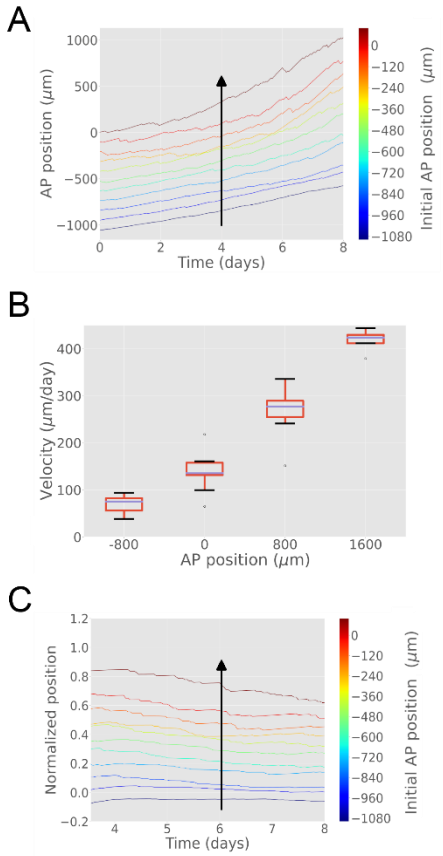

Figure 2-figure supplement 2. The model encompasses the cell pushing mechanism: the more posterior a cell is, the faster it moves. A) Cells located close to the amputation plane end up at the posterior end of the regenerated modelled tissue. B) Clones velocity monotonically increases with AP coordinate. Box plot representation showing median of clone velocities binned every 800 μm **C) Scaling behavior: clone cells preserve their original spatial order.** Relative position of each clone to the highly proliferating tissue delimited by its outgrowth and the recruitment limit remains constant in time. The figure depicts 11 simulations.

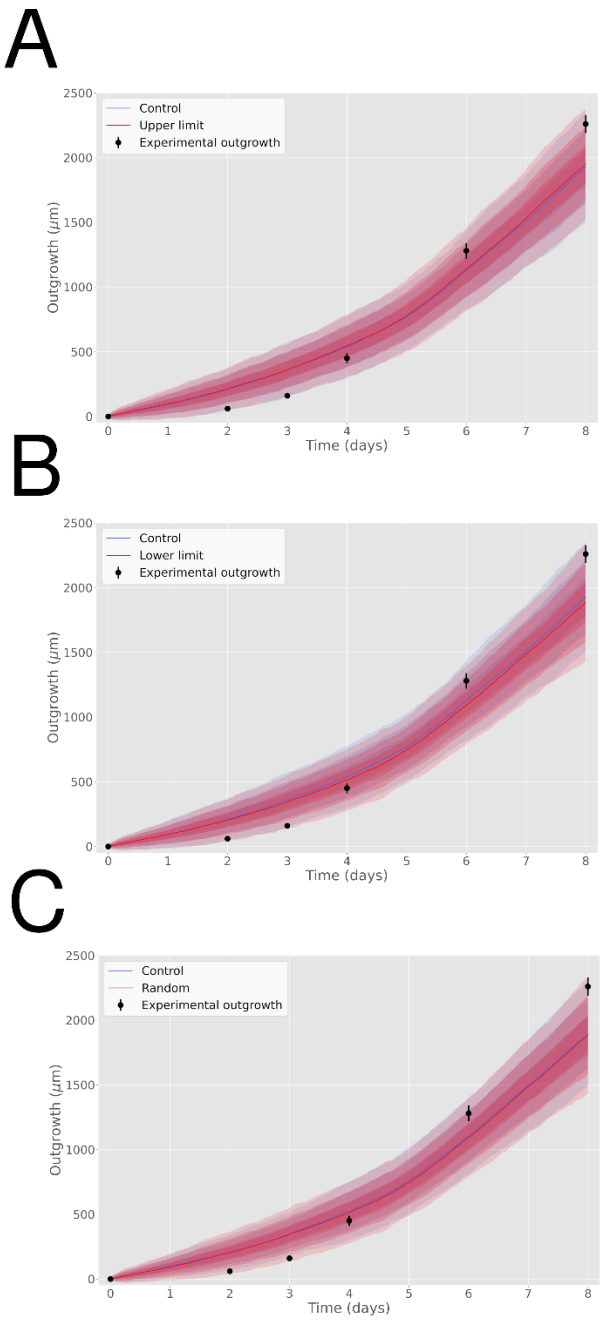

Figure 2-figure supplement 3. Incorporating variability of cell length along the AP axis does not impact on predicted axolotl spinal cord outgrowth. (A) Outgrowth predicted from the model assuming ependymal cell lengths equal to the experimental mean value plus three sigma of their cell length measured along the AP axis (in red). **(B)** Outgrowth predicted from the model assuming ependymal cell lengths equal to the experimental mean value minus three sigma of their cell length measured along the AP axis (in red). **(C)** Outgrowth predicted from the model assuming ependymal cell lengths extracted from a normal distribution parametrized from the experimental cell length measured along the AP axis (in red). In the three panels it is depicted the outgrowth predicted from the model assuming ependymal cell lengths equal to the experimental mean value of their cell length measured along the AP axis (Control, in blue, same simulations shown in Figure 2B). Experimental ependymal cell length along the AP axis are characterized by μ = 13.2 μm, σ = 0.1 μm.

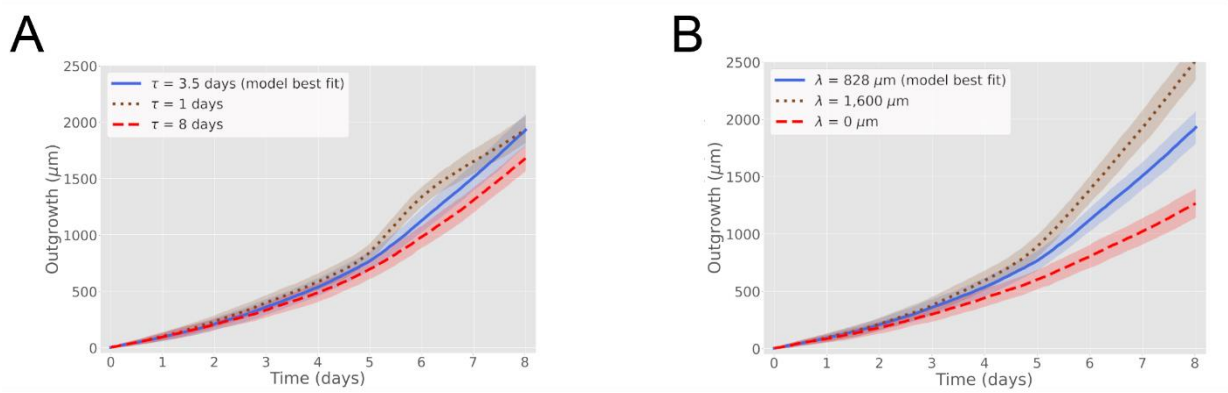

Figure 2-figure supplement 4. The maximal recruitment time (τ) and the maximal recruitment length (λ) determine the outgrowth of the axolotl spinal cord. A) Increase (decrease) of τ reduces (increases) the model-predicted spinal cord outgrowth. Time course of spinal cord outgrowth predicted by the model when varying τ from 1 day (brown) to 8 days (red). In blue, the prediction of the model assuming τ = 85 ± 12 hours. N_0 = 196 ± 2 cells and λ = 830 ± 30 μm. **B) Increase (decrease) of λ increases (reduces) the model-predicted spinal cord outgrowth.** Time course of spinal cord outgrowth predicted by the model when varying λ from zero (red) to 1,600 μm (brown). In blue, the prediction of the model assuming λ = 828 ± 30 μm. N_0 = 196 ± 2 cells and τ = 85 ± 12 hours. Simulations depicted in the blue curves in A and B are the same simulations shown in Fig. 2B. Means are depicted as lines while shaded areas correspond to 68 % confidence intervals, respectively, calculated from 1000 simulations.

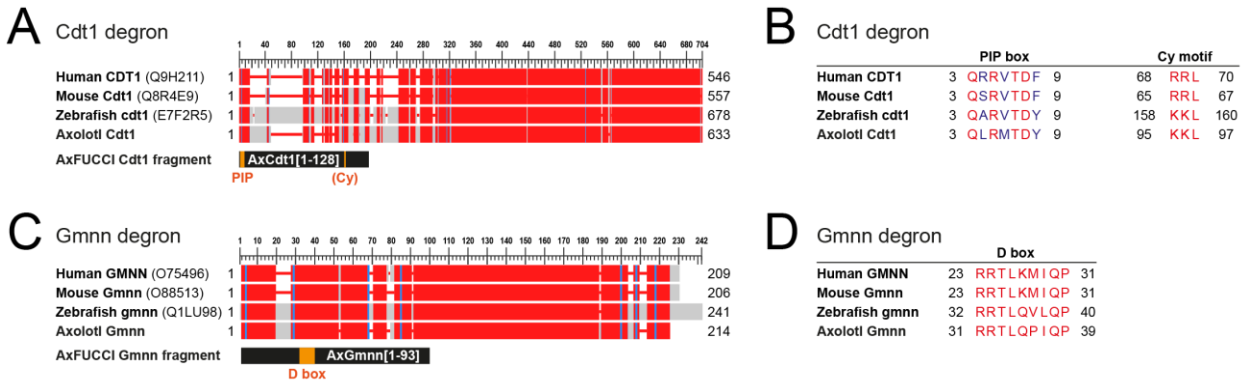

Figure 3-figure supplement 1. Determination of Cdt1 and Gmnn fragments for AxFUCCI reporter. A) Alignment of full length Cdt1 proteins from human, mouse, zebrafish and axolotl. Uniprot identifiers are given in parentheses. Numbers indicate amino acid residue numbers. Red regions indicate high amino acid similarity/identity; grey regions indicate low conservation. Alignments were performed using COBALT (NCBI). The AxFUCCI Cdt1 fragment comprises amino acids 1-128 of axolotl Cdt1, harboring the PIP box degron and corresponding to amino acids 1-190 of zebrafish cdt1 used to make zebrafish FUCCI (Sugiyama *et al.,* 2009, Bouldin *et al.*, 2014). **B) Amino acid alignments at the Cdt1 degron sequences.** The PIP box is well conserved evolutionarily. Like zebrafish cdt1, axolotl Cdt1 harbors a 'KKL' motif rather than the 'RRL' motif found in human and mouse. **C) Alignment of full length Gmnn proteins from human, mouse, zebrafish and axolotl.** The AxFUCCI Gmnn fragment comprises amino acids 1-93 of axolotl Gmnn, harboring the Destruction (D) box and corresponding to amino acids 1-100 of zebrafish gmnn1 used to make zebrafish FUCCI (Sugiyama *et al.,* 2009, Bouldin *et al.*, 2014). **D) Amino acid alignments at the Gmnn D box.**

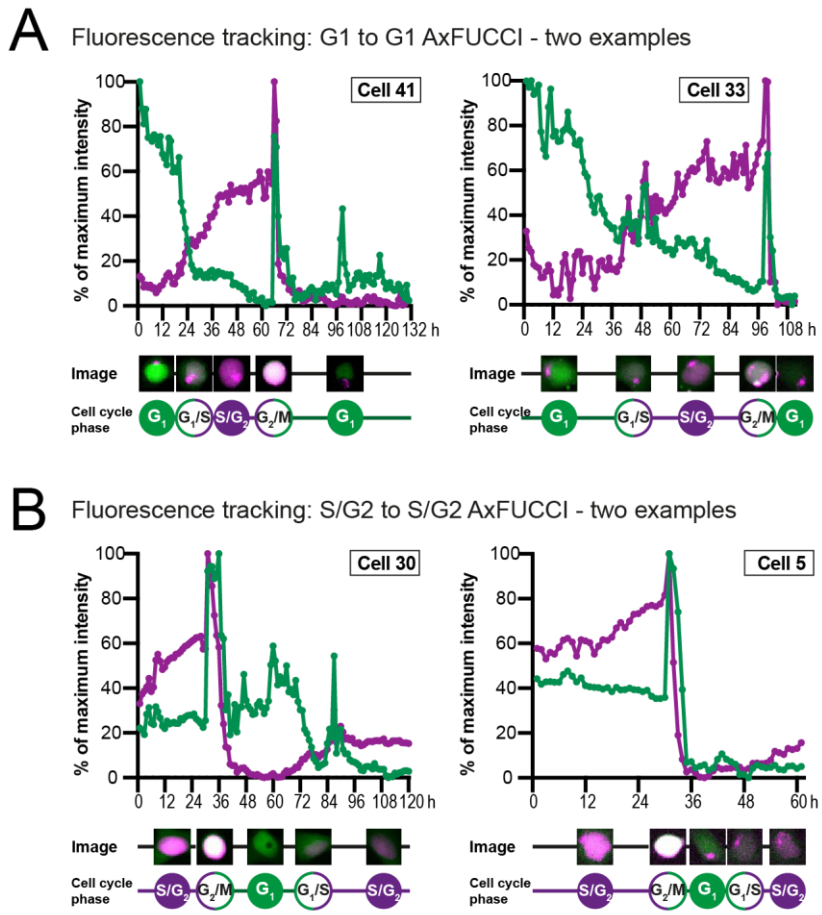

Figure 3-figure supplement 2. Fluorescence intensity measurements of AxFUCCI through the cell cycle. Fluorescence intensity measurements of AxFUCCI-electroporated AL1 cells as they transited through one cell cycle from G1 to the following G1 (**A**) or S/G2 to the following S/G2 (**B**). Two examples are presented for each transition. Green lines represent G0/G1-AxFUCCI fluorescence; magenta lines represent S/G2-AxFUCCI fluorescence. For each time point, the cell nucleus was segmented and the mean fluorescence intensity calculated. Fluorescence intensities were normalized to the maximal fluorescence value observed during the imaging session. h: hours after start of imaging. Maximum fluorescence is observed at mitosis, when the cell rounds up in preparation for cell division. Mean fluorescence intensity decreases sharply after each mitosis due to fluorophore and plasmid dilution between the two daughter cells. For sample videos, see Videos 2 and 3.

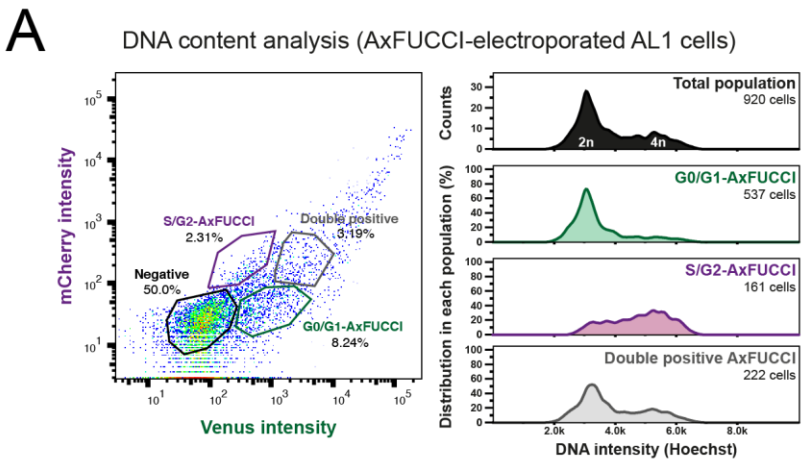

Figure 3-figure supplement 3. A) DNA quantification by flow cytometry to validate AxFUCCI functionality. A) Relative DNA content in G0/G1-AxFUCCI (green), S/G2-AxFUCCI (magenta) or Transition-AxFUCCI (grey) cells. AxFUCCI-electroporated AL1 cells were incubated with Hoechst DNA stain-containing cell culture medium for 90 minutes prior to dissociation and analysis.

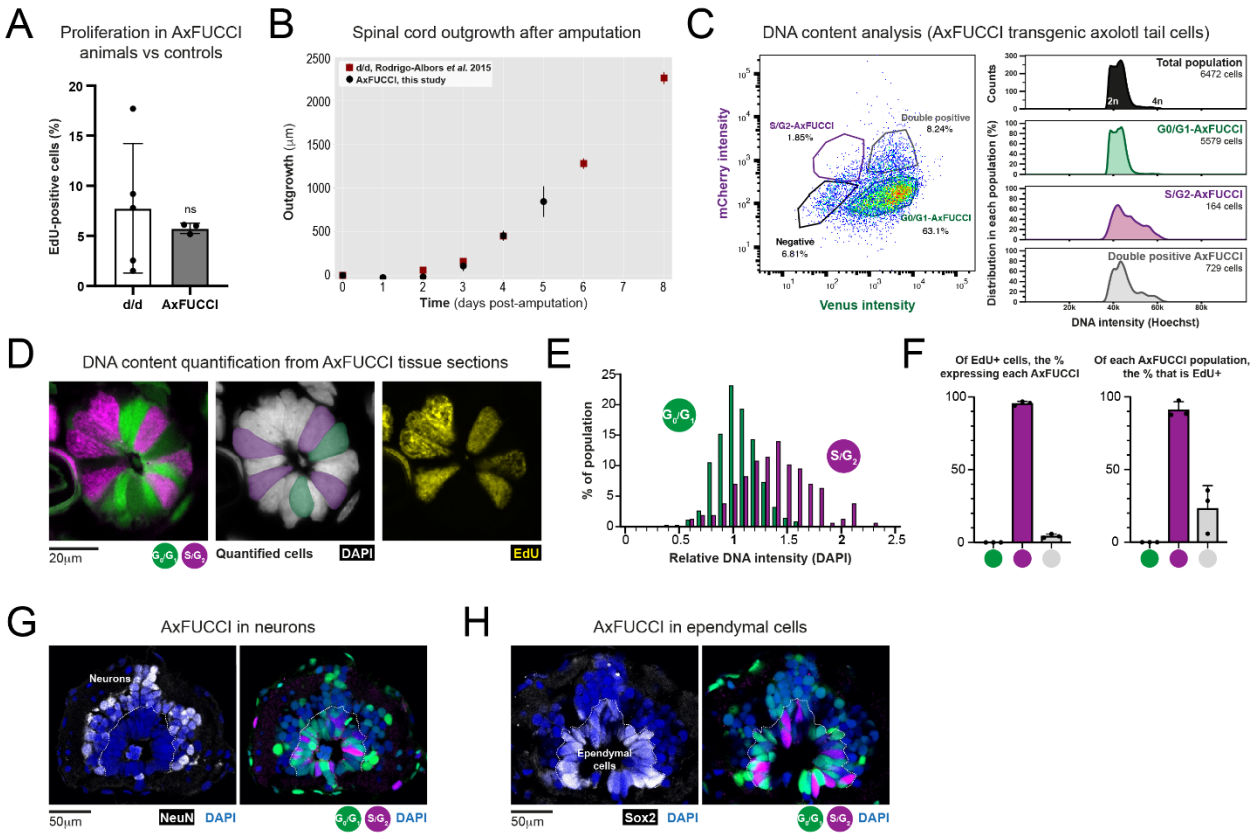

Figure 3-figure supplement 4. Validation of AxFUCCI functionality through *in vivo* tissue analysis. A) Baseline proliferation in AxFUCCI spinal cord is not significantly different from d/d controls. EdU was administered in a 2 hour pulse to uninjured AxFUCCI or d/d control animals. Tails were harvested and sectioned to quantify EdU-labelled proliferative cells in the spinal cord. ns: not significant, p=0.62 (two sample t-test). Error bars indicate standard deviation. n=5 tails (control) or 3 tails (AxFUCCI), 750 cells counted in total for each, of which ~50 cells were EdU-labelled. **B) AxFUCCI tails regenerate with normal kinetics.** Spinal cord outgrowth was measured every day up to 5 days after AxFUCCI tail amputation, and plotted together with measurements previously obtained from *d/d* control animals (Rodrigo-Albors *et al.*, 2015). **C) DNA quantification by flow cytometry.** Relative DNA content in G0/G1-AxFUCCI (green), S/G2-AxFUCCI (magenta) or Transition-AxFUCCI (grey) cells dissociated and harvested from uninjured AxFUCCI axolotl tails. Cells were incubated with Hoechst DNA stain for 60 minutes prior to analysis. **D) DNA quantification from AxFUCCI tissue sections.** Single section confocal image of a 10µm thick AxFUCCI spinal cord cross-section, co-stained with DAPI (grey) to label DNA. The DNA intensity of G0/G1-AxFUCCI cells (green) was compared to that of S/G2-AxFUCCI cells (magenta). The center panel depicts the cells that satisfy the criteria for quantification – they must span the spinal cord, contact the lumen and not be obscured by neighbouring cells. The AxFUCCI animals were also pulsed with EdU for 8 hours prior to tail harvesting. S/G2-AxFUCCI cells, but not G0/G1-AxFUCCI cells, incorporated EdU (yellow, right panel). **E) Histogram depicting the DAPI intensities of AxFUCCI cells quantified in D.** The mean intensity of G0/G1-AxFUCCI cells was set to an arbitrary value of 1 (2n). S/G2-AxFUCCI cells have a significantly higher DNA content than G0/G1-AxFUCCI cells (p=2.20x10^{-16}, Welch's test). n=3 tails (a total of 341 G0/G1-AxFUCCI cells vs 157 S/G2-AxFUCCI cells). **F) Correlation of EdU labelling (see panel D) with each AxFUCCI-expressing population.** n=3 tails, 819 AxFUCCI-expressing cells were counted in total, of which 171 had incorporated EdU. **G) Spinal cord neurons express G0/G1-AxFUCCI.** NeuN-expressing neurons are located on the periphery of the spinal cord. 98±1.5% of neurons expressed G0/G1-AxFUCCI, and the remainder did not express any AxFUCCI. n=5 tails, a total of 2,170 NeuN+ cells counted. **H) Ependymal cells express all AxFUCCI combinations.** Sox2-expressing ependymal cells are located on the interior of the spinal cord, lining the lumen.

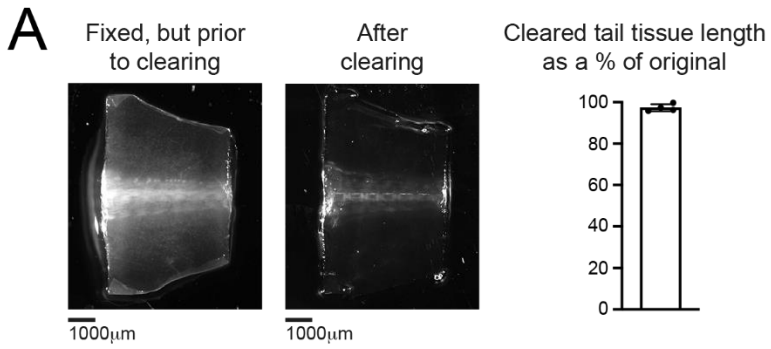

1246

1247 **Figure 3-figure supplement 5. The tissue clearing protocol does not alter spinal cord length. A)** The same, fixed
1248 tail tissue imaged prior to (left) or following (center) tissue clearing and refractive index matching. Right: Cleared
1249 tail tissue preserves 97±1.7% of its length compared to uncleared tail tissue. *n*=3 tails.

1250

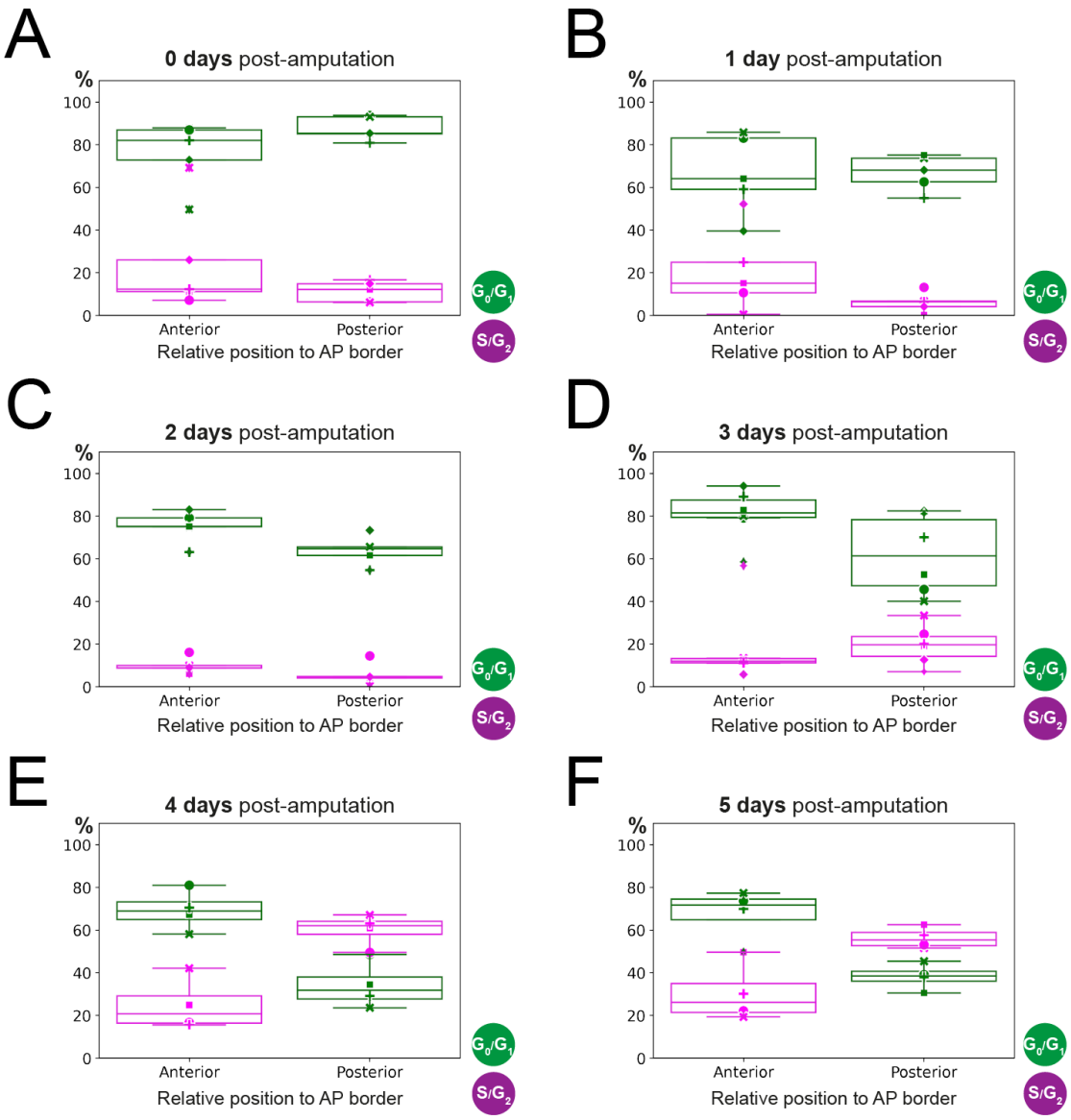

1251

1252 **Figure 4-figure supplement 1. Estimation of anterior and posterior percentages of G0/G1-AxFUCCI and S/G2-**
1253 **AxFUCCI expressing cells by fitting a two-zones model**. Dots correspond to the best-fitting value of the
1254 parameters $g0g1_a$, $g0g1_p$, $sg2_a$ and $sg2_p$ to the experimental spatial AP profiles of the percentages of G0/G1-
1255 AxFUCCI (in green) and S/G2-AxFUCCI (in magenta) expressing cells for each animal, at each timepoint **(A-E)**. Each
1256 symbol identifies a different animal (same criteria as in Figure 4). Box plots show that at day 0 to 3 days post-
1257 amputation, anterior and posterior values are not significantly different from each other (A - D). In contrast, at day
1258 4 and 5, anterior and posterior values are significantly different (E, F) (Kolmogorov-Smirnov test p = 0.0286)
1259 (Materials and method section 2.12 for more details).

1260

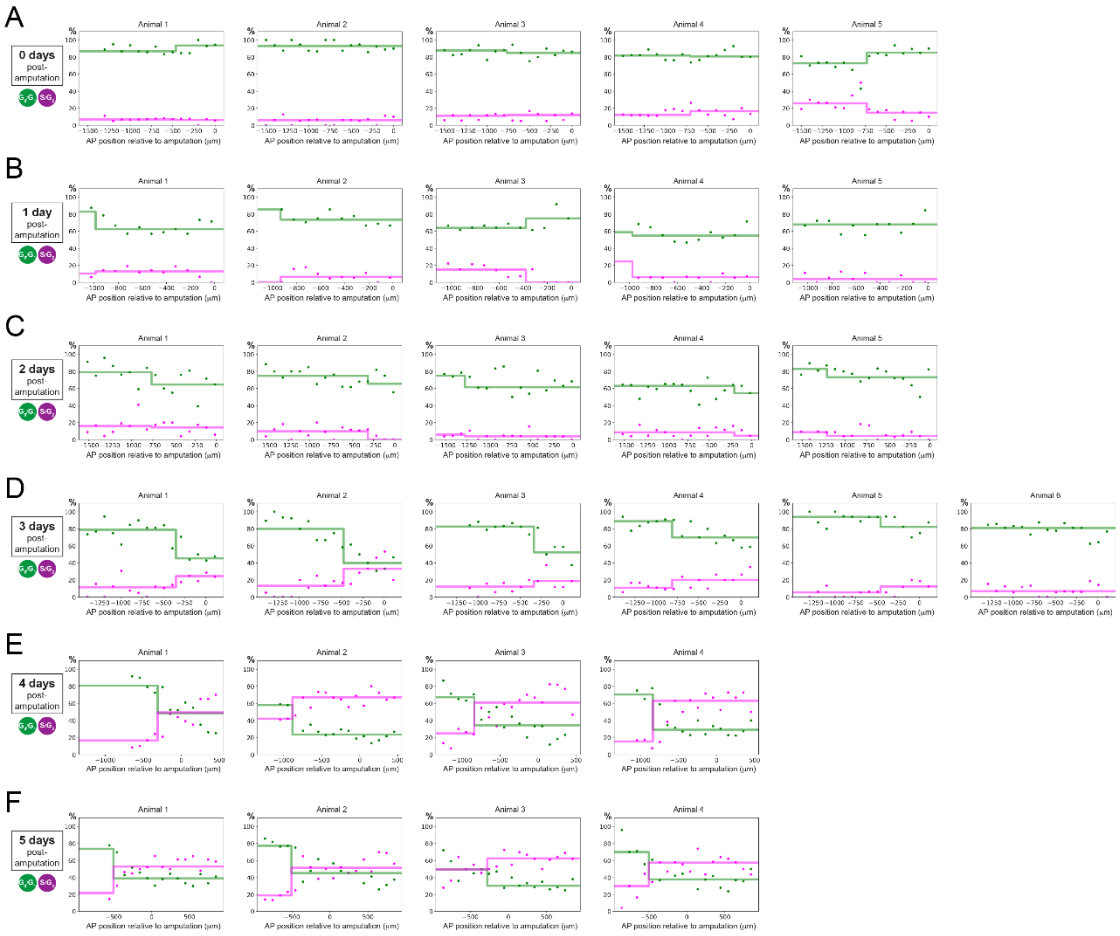

1261

1262 **Figure 4-figure supplement 2. Individual fitting of the two-zones model to experimental AP profiles of the**
1263 **percentages of G0/G1-AxFUCCI and S/G2-AxFUCCI expressing cells**. Percentage of G0/G1 (in green) and S/G2 (in
1264 magenta)-AxFUCCI-expressing cells quantified in 100 µm bins along the anterior-posterior spinal cord axis. A
1265 mathematical model assuming two adjacent spatially homogeneous zones separated by an anterior-posterior
1266 border (AP border) was fitted to the G0/G1 and S/G2-AxFUCCI-data for each animal at time 0 **(A)**, 1 **(B)**, 2 **(C)**, 3 **(D)**,
1267 4 **(E)** and 5 **(F)** days post amputation. Anterior-posterior position is defined with respect to the amputation plane (0
1268 µm). Best fitting values of the model regarding the anterior and posterior percentage of AxFUCCI data is in Figure 4
1269 – figure supplement 1 (For more details, see Materials and Methods section 2.12).

1270

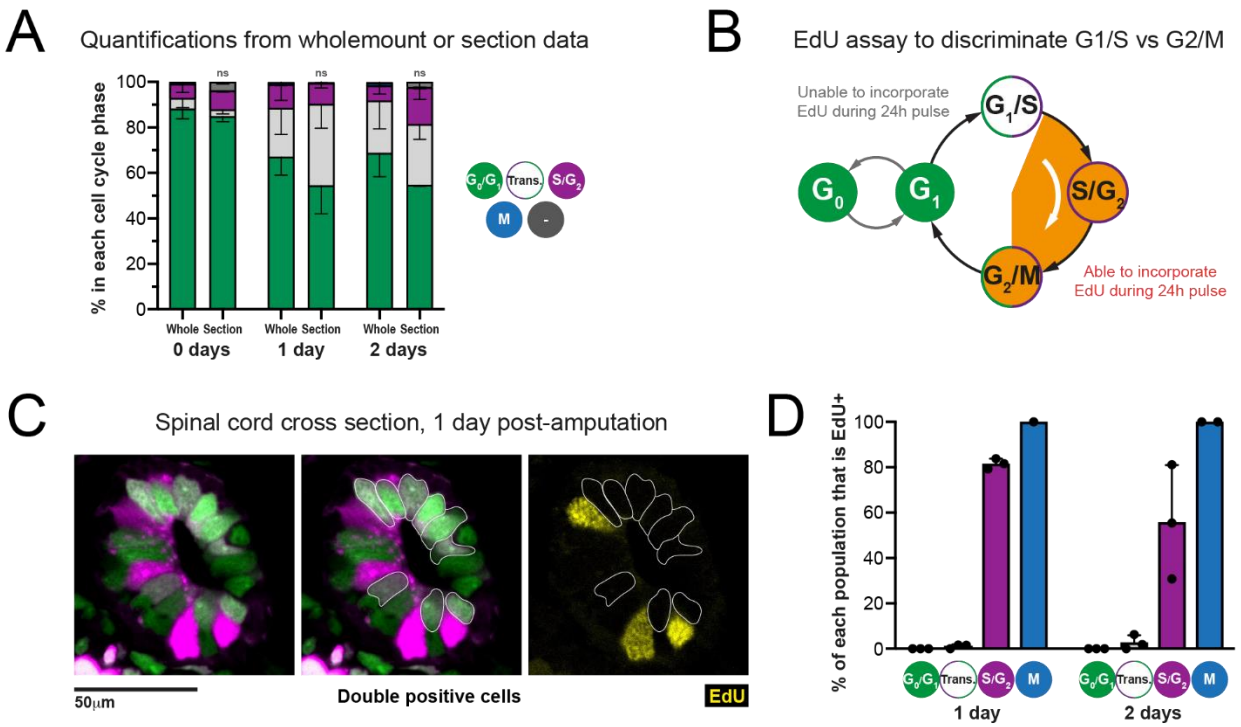

Figure 5-figure supplement 1. Transition-AxFUCCI cells at 1 and 2 days post-amputation reside at the G1/S boundary. A) Comparison of AxFUCCI quantifications made from wholemount specimens (Whole) or tissue sections (Section). No difference was observed between wholemount-based quantifications and section-based quantifications (one way ANOVA). *n*=3 tails per time point, ~400 cells counted in each, corresponding to ~750µm of spinal cord. Error bars indicate standard deviation. **B) EdU-based assay to distinguish G1/S cells and G2/M cells. C) Single 10µm section confocal image of a spinal cord at 1 day post-amputation, pulsed for 24 hours with EdU prior to harvesting.** Transition-AxFUCCI cells (double positive, outlined) have not incorporated EdU (yellow). Neighbouring S/G2-AxFUCCI cells (magenta) have incorporated EdU (internal control). **D) The percentage of each AxFUCCI population and mitotic cells that incorporated EdU in the assay in B.** As expected, no G0/G1-AxFUCCI cells incorporated EdU and all mitotic cells had incorporated EdU. The majority of S/G2-AxFUCCI cells had incorporated EdU. In contrast, almost none of the Transition-AxFUCCI cells at 1 and 2 days post-amputation incorporated EdU, indicating that they reside at the G1/S transition. *n*=3 tails per time point. Total cells counted per time point: 1 day post-amputation [671 G0/G1-AxFUCCI, 115 S/G2-AxFUCCI, 442 Transition-AxFUCCI, 1 mitotic cell], 2 days post-amputation [643 G0/G1-AxFUCCI, 191 S/G2-AxFUCCI, 315 Transition-AxFUCCI, 3 mitotic cells].

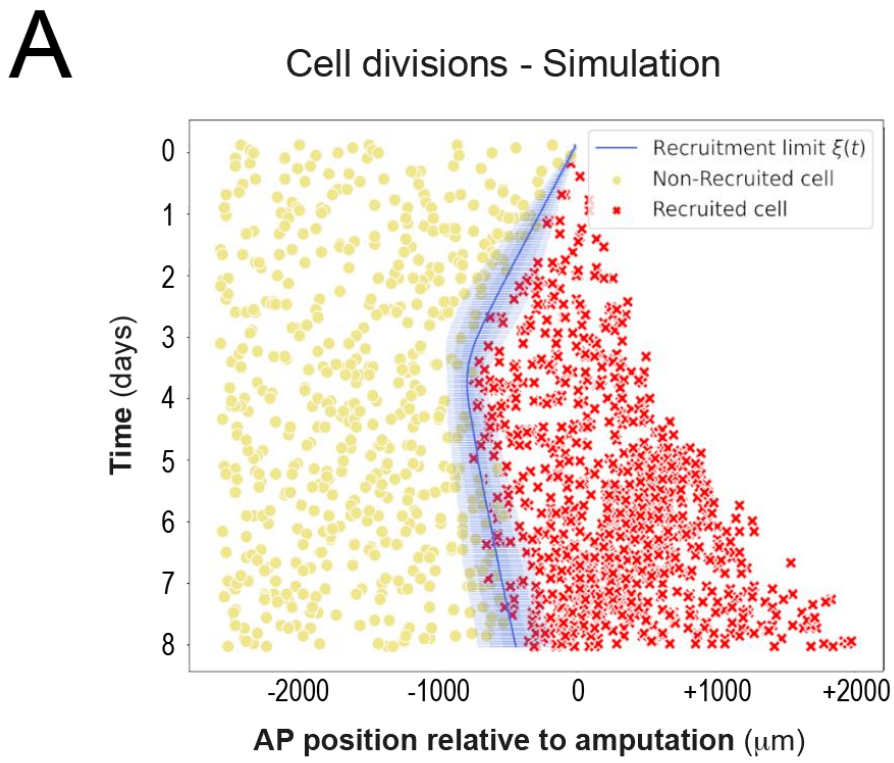

Figure 6 – figure supplement 1. Modelled spatiotemporal distributions of ependymal cell divisions during axolotl spinal cord regeneration. Model-predicted occurrence of cell divisions is more often within the recruited (red crosses) compared to the non-recruited (yellow circles) cells, where recruited and non-recruited cells are separated by the recruitment limit $\xi(t)$. The model is parameterized as in Figure 2 and Figure 6 C-E.

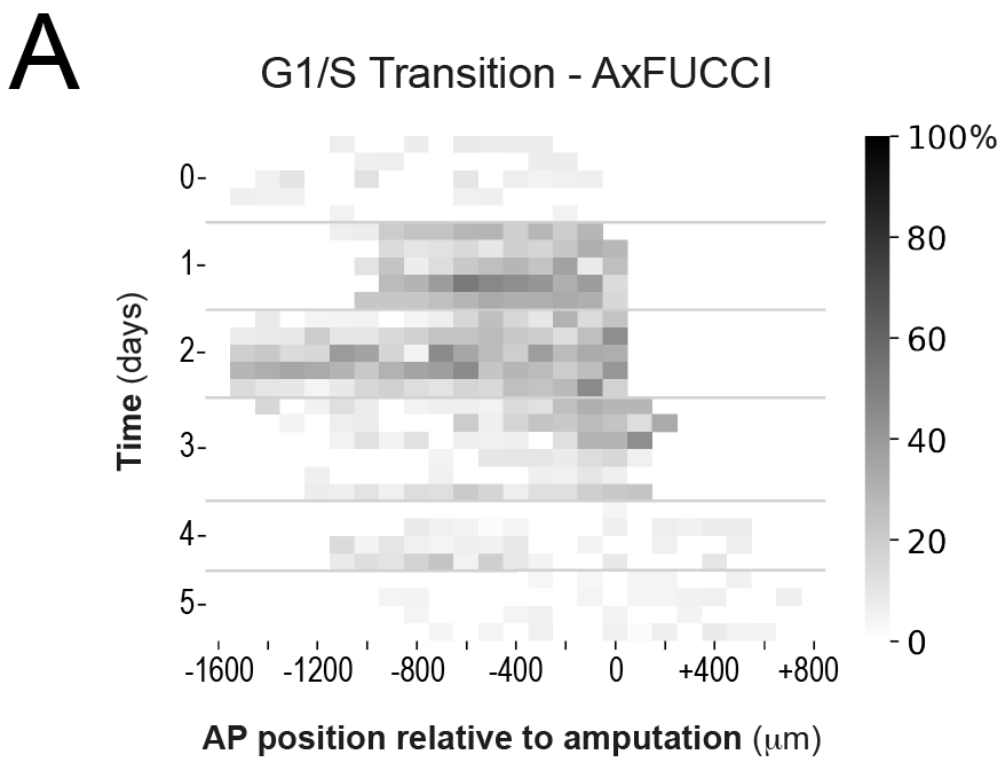

1293

1294 **Figure 6 – figure supplement 2. Spatiotemporal distributions of Transition AxFUCCI cells during axolotl spinal**
1295 **cord regeneration.** Heatmaps depicting experimental spatiotemporal distribution of Transition AxFUCCI cells.
1296 Anterior-Posterior (AP) position is depicted horizontally with respect to the amputation plane (AP position = 0 μm).
1297 In the vertical axis time from amputation (Time = 0 days) and experimental replicates within each time. The color
1298 code corresponds to the percentage of Transition AxFUCCI cells. The increase in Transition AxFUCCI cells at days 1
1299 and 2 post-amputation is readily observed.

1300

Video legends

Video 1. 1D Model simulations of spinal cord regeneration. **Top panel)** 20 model simulations from 20 different random seeds (the seeds are shown in the vertical axis). The color code corresponds to the generation of each cell (blue, orange and black correspond to the first, second and third generation, respectively). Vertical interrupted black line denotes the amputation plane (AP coordinate of 0). The recruitment limit ξ(t) (vertical red dashed line) propagates linearly in time up until the time τ of 85 hours post amputation, covering up the maximal recruitment λ of 828 μm anterior to the amputation plane. **Bottom left panel)** Predicted recruitment limit ξ(t) as a function of time from the simulations showed in the top panel). Mean value is depicted in the red line while the red shaded areas corresponds to 68, 95 and 99.7 % confidence intervals **Bottom right panel)** Predicted spinal cord outgrowth predicted by the model from the simulations showed in the top panel). The line represents to the mean (also indicated as the blue vertical line in the top panel) and the blue shaded areas correspond to the 68, 95 and 99.7 % confidence intervals. The 20 simulations have the same parametrization than the 1,000 simulations showed in Figure 2A and Figure 2B.

Video 2. Live imaging of an AxFUCCI-electroporated AL1 cell (G1 to G1). A single AxFUCCI-electroporated AL1 cell passing through one cell cycle from G1 to G1, imaged hourly over ~130h. The cell transitions through the cell cycle phases in the following order: Green (G0/G1-AxFUCCI) > White (Transition-AxFUCCI) > Magenta (S/G2-AxFUCCI) > White (Transition-AxFUCCI) > Mitosis > Two Green daughter cells (G0/G1-AxFUCCI). This cell corresponds to Cell 41 tracked in Figure 3 - figure supplement 2. Fluorescence intensity drops after mitosis due to fluorophore and plasmid dilution (non-integrating transgene).

Video 3. Live imaging of an AxFUCCI-electroporated AL1 cell (S/G2 to S/G2). A single AxFUCCI-electroporated AL1 cell passing through one cell cycle from S/G2 to S/G2, imaged overly over ~120h. The cell transitions through the cell cycle phases in the following order: Magenta (S/G2-AxFUCCI) > White (Transition-AxFUCCI) > Mitosis > Two Green daughter cells (G0/G1-AxFUCCI) > White (Transition-AxFUCCI) > Magenta (S/G2-AxFUCCI). This cell corresponds to Cell 30 tracked in Figure 3 - figure supplement 2. Fluorescence intensity drops after mitosis due to fluorophore and plasmid dilution (non-integrating transgene).

Video 4. 3D imaging of an optically cleared AxFUCCI tail tip. Volume rendering of a fixed and optically cleared AxFUCCI tail tip, co-stained for DNA using DAPI (blue) and imaged with a lightsheet microscope. The spinal cord is visible as an intensely green and magenta rod at the center of the sample. Peripheral signal is AxFUCCI expression in surface epidermal cells. Other internal structures, including notochord, have weaker AxFUCCI expression and are not visible in this rendering. Volume rendering was performed using Imaris software. See also Figure 3D.

Video 5. 1D Model simulations of spinal cord regeneration showing cells in G1 and S phases. 20 model simulations from 20 different random seeds (the seeds are shown in the vertical axis). Cells in G1 and S are depicted in green and magenta, respectively. Predicted recruitment limit ξ(t) and outgrowth are indicated with the vertical red and blue discontinuous lines, respectively. Amputation plane is depicted as a vertical black dashed line. The simulations have the same parametrization than the simulations showed in Figure 2A and Figure 2B.

1341 **Tables**

1342

1343 **Table 1.** Model parameters.

Model parameter	Value / explanation	Fixed/Free
G1 phase non-regenerating mean	152 hours	Fixed parameters, extracted from Rodrigo Albors *et al.*, 2015.
G1 phase non-regenerating sigma	54 hours	
S phase non-regenerating mean	179 hours	
S phase non-regenerating sigma	21 hours	
G2 + M phases non-regenerating mean	9 hours	
G2 + M phases non-regenerating sigma	6 hours	
G1 phase regenerating mean	22 hours	
G1 phase regenerating sigma	19 hours	
S phase regenerating mean	88 hours	
S phase regenerating sigma	9 hours	
G2 + M phases regenerating mean	9 hours	
G2 + M phases regenerating sigma	2 hours	
GF non regenerating	0.12	
Cell length along the AP axis	13.2 μm	
$t_{G0\text{-}G1}$	48 72 hours	
N_0	Initial number of cells along the AP axis, anterior to the amputation plane.	Free parameters (determined in this study).
λ	Maximal length from the amputation plane recruited by the signal (μm).	
τ	Maximal time for cell recruitment (days after amputation or hours after amputation).	

1344

1345

1346 **Table 2.** Primers used in this study.

1347

Primer name	Sequence	Purpose
axCdt1-fwd	TCAT**GCGGCCGC**ATGGCCCAGCTCCGGATGA	Forward primer to amplify axCdt1[aa1-128] from axolotl embryonic cDNA. Bold indicates a NotI restriction site.
axCdt1-rev	TCAT**GCTAGC**GAATTCTCCGCTTCCTGCTGCGCTTCCTGCGCTTCCCAGGGATGATGGGGTTAATGGCT	Reverse primer to amplify axCdt1[aa1-128] from axolotl embryonic cDNA. Bold indicates a NheI restriction site. Underlined sequence encodes GS-rich linker.
Venus-fwd	TCAT**GCTAGC**ATGGTGAGCAAGGGCGAGG	Forward primer to amplify mVenus sequence from addgene plasmid #27793. Bold indicates a NheI restriction site.
Venus-rev	TCAT**ACCGGT**CTTGTACAGCTCGTCCATGCC	Reverse primer to amplify mVenus sequence from addgene plasmid #27793. Bold indicates a AgeI restriction site.
axGmnn-fwd	TCAT**TCCGGA**GGAGGAGGAGGAAGCGGAGGAGGAGGAAGCATGAATGCTAAGAAAGCAGCGACAAT	Forward primer to amplify axGmnn[aa1-93] from axolotl embryonic cDNA. Bold indicates a BspEI restriction site. Underlined sequence encodes GS-rich linker.
axGmnn-rev	TCAT**ATCGAT**GCTGTAAGCTTCTTGGGACACCC	Reverse primer to amplify axGmnn[aa1-93] from axolotl embryonic cDNA. Bold indicates a ClaI restriction site.

1348